Mechanics of Spinal Cord Decompression Sickness

by

Roman Alvarado

A dissertation submitted in partial fulfillment
of the requirements for the degree of
Doctor of Philosophy
(Biophysics)
in the University of Michigan
2024

Doctoral Committee:

Professor Jens-Christian Meiners, Chair
Professor Jordan Horowitz
Professor Zhen Xu
Professor Michal Zochowski

Roman Alvarado
alvarro@umich.edu
ORCID iD: 0000-0002-8354-8631

ACKNOWLEDGEMENTS

I would like to express my deepest appreciation to my research advisor and chair, Prof. Jens-Christian Meiners. Prof. Meiners has taught me how to be an effective researcher and has instilled confidence in my skillset. I could not have asked for a better advisor.

I would also like to thank the remaining members of my committee: Prof. Jordan Horowitz, Prof. Michal Zochowski, Prof. Zhen Xu. They provided excellent feedback and helped steer the direction of this project.

I would also like to thank the following individuals for their guidance: Ulrich Scheven and Joan Greve for their magnetic resonance imaging expertise; Tejaswi Worlika and Cameron Hodges for their help with bubble imaging and getting started in the lab; Joshua Kooistra, Xiaoxuan Zhang, and Krishna Garikipati for their contributions to setting up the finite-element model of the spinal cord; the University of Michigan machine shop staff for their assistance in iterating many designs for multiple projects; and Jonathan Sukovitch and Zhen Xu for allowing us to use their lab space on North Campus. I would also like to extend my gratitude to Osama Kashlan for helping prepare histology samples and to Angela Yee for teaching me how to handle animals. And, of course, I am grateful for the many undergraduate members of my research group over the years who enriched the lab experience.

Next, I'd like to express my deepest gratitude to my wife, Allison Alvarado, and to my friends and family for their continual support and encouragement throughout my journey. I would not have been able to accomplish this without their unwavering belief in me.

I am very grateful for the funds provided by the Divers Alert Network and from the University of Michigan to support me and the work presented in this dissertation.

Finally, I would like to acknowledge the sacrifice of all the animals used in this study, as without them the advancement of scientific knowledge would be greatly impeded.

TABLE OF CONTENTS

LIST OF FIGURES

LIST OF TABLES

TABLE

LIST OF APPENDICES

LIST OF ACRONYMS

ATA: Absolute Atmosphere

MR(I): Magnetic Resonance (Imaging)

(SC-)DCS: (Spinal Cord) Decompression Sickness

SD: Standard Deviation

SEM: Standard Error of the Mean

SM: Solid Mechanics

TDS: Transport of the Diluted Species

ABSTRACT

Decompression sickness (DCS), also known as "the bends," is a complex and multifaceted condition that arises from rapid changes in ambient pressure, leading to the formation of nitrogen gas bubbles in the body. Among various tissues, injury to the spinal cord is especially susceptible to the devastating effects of DCS. To better understand the etiology of spinal cord decompression sickness (SC-DCS), it is first necessary to understand the interaction between gas and tissue mechanics in the context of decompression bubbles.

We used ex vivo bovine spinal cord tissues to study the bubble-tissue mechanics with cyclic pressure changes. With each progressive pressure cycle, the bubble irreversibly expanded, indicating mechanical damage to ex vivo bovine spinal cord tissue caused by growing decompression gas bubbles. This behavior cannot be explained by the assumed reversible elastic response of the surrounding tissue. These results underscore the importance of considering SC-DCS as a complex condition that requires a comprehensive approach in its treatment.

To further support and explain the ex vivo data, we developed a coupled tissue-gas mechanics model. The model behaved differently at different timescales, under different decompression profiles, and with varying seed bubble sizes. Our analysis revealed several key insights: (1) tissue mechanics plays a significant role in the resulting average surface stress of bubbles during decompression (2) that recompression can result in a similar stress profile as decompression, and (3) diffusion effects dominate decreasing bubble sizes while tissue mechanics dominate larger bubbles. The combined effect of these mechanics leads to a diverse range of possible dynamic behaviors in decompression bubbles and tissue.

To examine decompression bubbles natively, we developed a novel compression chamber compatible with rodent vital monitoring and real-time magnetic resonance imaging. We

maintained adequate anesthetic depth in our rodents and identified various locations for these bubbles, including potential hemorrhaging. This system enables us to test many empirical recommendations for managing SC-DCS and quantify their effect on the spinal cord.

Our research provides a solid foundation for the development of new, safe decompression models for aeronautical and diving activities based on physiologically relevant biophysical principles. The combination of our experimental and theoretical tools can pave the way for a more comprehensive understanding of SC-DCS and its management.

CHAPTER 1

Introduction

Humans have always ventured into extreme environments—whether diving to deep depths, mining for valuable resources, or conquering the skies and space—each are subject to changes in ambient pressure. It wasn't until the 19th century that records began to describe severe joint pain, fatigue, and more alarming symptoms like paralysis among miners who returned to normal atmospheric pressure [3, 4]. This mysterious condition became infamously known as "the bends," named after the agonizing posture construction workers adopted during projects like the St. Louis Bridge and the Brooklyn Bridge [3, 4, 5]. As these symptoms appeared in a range of pressurized environments, it became evident that a quick transition from high pressure to normal conditions was the culprit.

Decompression sickness (DCS), or "the bends," is a physiological response to rapid decreases in pressure, where nitrogen gases once dissolved in the blood and tissues come out of solution because of supersaturation during decompression, forming bubbles [6, 4]. And although the nucleation sites for these bubbles are not well understood, the proportional relationship between gas partial pressure and the gas concentration at the tissue-liquid interface is well-described by Henry's law [7, 8]. Understanding the delicate balance between pressure, dissolved gases, and the formation of bubbles is crucial to preventing the potentially devastating effects of DCS that involve reduced ambient pressure [9, 10].

Despite over a century of research, the underlying mechanisms of this condition remain elusive. This is partly because decompression bubbles circulate throughout the human body

and enter a variety of tissues or form in deep tissues [11], each with its own unique parameters. An inexhaustive list includes the observation of bubbles or pain in joints and bones [12, 13], skin [14, 15], and the spinal cord [16, 17]. However, two main types of DCS have been softly identified. Milder symptoms that can resolve spontaneously are referred to as DCS Type 1 [18], while the more life-threatening symptoms, including neurological disruption, are referred to as Type 2 DCS [19]. Among neurological tissues, the spinal cord is especially susceptible to Type 2 DCS is the spinal cord [20], being up to six times more affected than other tissues [21]. This increased vulnerability is thought to be due to a fourfold faster perfusion rate through the blood-brain barrier compared to the slow-flowing drainage found in the spinal cord [22, 23]. It is this reason that this dissertation focuses on spinal cord decompression sickness (SC-DCS).

Regardless of the tissue affected by DCS, there is no consensus on the primary mechanism underlying the physiological response to bubbles. Several studies have noted complement activation [24, 25] and disruption to the endothelial layer [26, 27, 28]. Generally, it is assumed bubbles damage surrounding tissues by blocking blood flow [Manabe 1998] or compressing tissues [29], eventually leading to ischemia. This assumption has justified various treatment methods aimed at reducing bubble size to prevent ischemia.

The primary treatment for DCS is hyperbaric recompression therapy, which recompresses the patient with intermittent phases of oxygen administration. Oxygen improves the resolution rate of inert gas bubbles by creating a lower concentration of nitrogen in the bloodstream relative to nitrogen-saturated tissues [30]. According to theoretical dissolution models [31], hyperbaric recompression therapy should effectively remove bubbles within hours after recompression, although it is only partially effective in practice [32, 33].

To justify experimental treatment methods, bubble classification systems have been used to correlate the severity of DCS with the presence of bubbles in the bloodstream [34, 35]. Ultrasound is the most common method to visualize bubbles [36, 37, 38], but the presence of bubbles in large arteries is not a reliable diagnostic indicator for diagnosing DCS [37]. Several

studies have used MRI to observe spinal cord disruptions due to DCS in humans [39, 40, 41], although these are retrospective studies. Additionally, using MRI to diagnose DCS remains controversial, as the standard recommendation is to initiate hyperbaric recompression therapy as quickly as possible [42] and there is no standardized imaging protocol [43]. This may explain the controversial results regarding clinical sensitivity in patient evaluation [39, 44].

Other researchers have focused on creating safe decompression tables using theoretical models. Haldane was the first to create decompression tables based on the assumption of limiting gas supersaturation during decompression [45]. The Haldane model assumed 16 independent tissue compartments with varying half-times to describe the exponential kinetics of gas perfusion. Since then, this model has been modified to incorporate more tissue compartments and longer half-times [46, 47] to improve safety. As a result, many of the operational dive tables today are built on Haldane's foundational model [48]. However, these models are empirical and are difficult to extend to non-tested dive scenarios [48], requiring users to select their own DCS risk [49] without considering the interaction of bubbles and tissues at different pressures.

It is clear that there are several limitations in the understanding of the mechanics of decompression bubbles in SC-DCS. The results presented aim to lay the foundation for future quantifiable, rather than empirical, research by providing a new mathematical framework that couples tissue-gas mechanics and a compression chamber compatible with MRI to visualize the growth and dissolution of decompression bubbles. The dissertation is organized as follows. Chapter 2 quantifies the irreversible damage caused by the expansion of decompression bubbles in ex vivo bovine spinal cord tissues. This experimental data is supported by a finite element model that couples gas and tissue mechanics. The analysis of this model is extended in Chapter 3. Our model analysis reveals that (1) the resulting stress from the interaction between tissue and bubble significantly changes under different decompression profiles, (2) recompression can result in comparable stresses to decompression, (3) small bubbles are dominated by gas diffusion while large bubbles are dominated by tissue me-

chanics in our chosen decompression profile. In Chapter 4, we discuss the development of a compression chamber for anesthetized rodents, designed to monitor vital signs and observe the growth of decompression bubbles in an MRI in real-time. Appendix A lists the electrical circuit schematics for the in vivo pressure chamber discussed in Chapter 3. Appendix B lists the standard operating protocol for operating the in vivo pressure chamber. Appendix C provides a LABVIEW front panel and block diagram for the in vivo pressure chamber.

CHAPTER 2

Mechanical Damage to Spinal Cord Tissue from Decompression Bubble Expansion

The pathophysiological mechanisms by which decompression gas bubbles damage the tissue are poorly understood. We present evidence from ex-vivo experiments and in-silico simulations that show that a growing gas bubble in the spinal cord can mechanically tear the surrounding nerve tissue. Experimentally, we observe bubble growth in spinal cord samples inside a pressure chamber with magnetic resonance imaging and probe the mechanical tissue response to rapid changes in pressure. We observe irreversible enlargement of the space occupied by the bubble upon pressure cycling, indicating tearing or viscoelastic deformation of the tissue. Computer simulations validate this finding by confirming that the forces involved in gas bubble growth are sufficiently large to exceed the tensile strength of the tissue. These findings suggest that mechanical damage to the spinal cord that is akin to a traumatic spinal cord injury is a possible injury mechanism in spinal cord decompression sickness, besides ischemic injury from blocked blood flow and immunologic reactions to the presence of the bubble.

2.1 Introduction

Decompression illness is a rare but serious condition that has a broad spectrum of clinical symptoms. It arises from a rapid drop in ambient pressure, most notably in sport and

commercial diving [9] and caisson construction work, but also in high-altitude aerospace operations [10], where space suits for extravehicular activities are pressurized to only 0.3 atmospheres. In its most severe and clinically challenging form, decompression sickness affects the central nervous system and especially the spinal cord. There are an estimated 1000 cases annually of spinal-cord decompression sickness (SC-DCS) in sport diving alone [50].

The pathophysiology of SC-DCS is poorly understood. While it is quite clear that the formation of inert gas bubbles in supersaturated tissue is the root cause, the actual mechanisms by which these bubbles damage the spinal cord are still largely shrouded in mystery. The presence of gas bubbles in the spinal cord has been amply established through histopathology in numerous animal experiments in which rats and other model animals were exposed to compression, tissue saturation, and rapid decompression to induce SC-DCS [51, 52]. From these experiments, three pictures of bubble formation in the spinal cord have been suggested: bubbles that lodge in the vascular microcapillaries and grow by accreting gas from the surrounding supersaturated tissue [29], bubbles that cause blockages on the venous side [53], and gas bubbles that nucleate and grow autochtenously in the extravascular tissue [54]. While the relative importance of these mechanisms is still controversial, it is often assumed that direct vascular blockage from the bubbles or indirect blockage from elastic mechanical forces associated with the bubbles lead to a local reduction in blood flow and thus an infarction of the spinal cord [55].

An alternative damage mechanism is direct, mechanical damage to the spinal cord from the expanding gas bubble. While this mechanism has been suggested in the past based on histopathologic examinations [51], compelling evidence for this mechanism has been scarce, in no small part because it is difficult to distinguish mechanical damage from a bubble from artifacts arising from the microtome slicing process in these studies [52, 29]. In this article, we show in non-destructive ex-vivo magnetic resonance imaging (MRI) experiments and complementary finite-element simulations that a growing decompression gas bubble can

directly cause irreversible mechanical damage to the surrounding spinal cord tissue. This suggests that SC-DCS may need to be understood not only as ischemic nerve damage, but also as a form of traumatic spinal cord injury and treated accordingly.

2.2 Materials and Methods

2.2.1 Sample Preparation

Bovine spinal cord was chosen as our model system because its tissue mechanical properties are similar to those of human spinal cords [1]. Fourteen spinal cords were obtained from a local commercial meat processor and immediately immersed in 0.9% saline solution on ice. From each spinal cord three samples of approximately 6 cm in length were cut from the thoracic or lumbar region, and the pia mater was removed. The samples were then placed into individual acrylic pressure chambers were they were immobilized at the bottom with a small amount of 2% low melting point agarose to prevent movement during compression and decompression.

2.2.2 Pressure Chambers and Initial Compression and Decompression

The pressure chambers were machined from solid acrylic. They have an inner diameter of 20 mm and a wall thickness of 9 mm. They are designed and tested to withstand pressures in excess of 15 bar. A non-metallic MRI-compatible fitting and Tygon tubing allows the pressurization and depressurization of the chamber inside or outside the MRI scanner.

After a sample is mounted inside the chamber, the chamber is purged with nitrogen at atmospheric pressure and sealed. The chamber is then pressurized to 7 bar (absolute) with nitrogen. Once pressurized, the chamber with the sample inside is placed in an ice bath for 48 hrs. to fully saturate the tissue sample with nitrogen. After this initial incubation

the pressure is rapidly lowered to 3 bar for 24 hrs. to induce bubble formation and let the bubbles reach mechanical and diffusive equilibrium with the surrounding tissue.

2.2.3 Magnetic Resonance Imaging

We are using a 7 T small animal MRI scanner (Varian) with a 310 mm bore to image the samples inside their pressure chamber. To minimize edge artifacts at the boundary between the bubble and the tissue, a two-dimensional T2-weighted fast spin echo (FSE) sequence was used (TE/TR = 36ms/5500ms, ETL = 8, FOV=2.5cm, views=512x256, slice thickness=800 um, and bandwidth = 227.27 kHz).

2.2.4 Pressure Cycling

To test the mechanical response of the tissue to bubble expansion, we rapidly cycled the external pressure while imaging the bubbles to determine any changes in their size and shape. Initial images were taken after 24 hours at 3 bar and then repeated to ensure no further bubble growth was occurring. This ensured that mechanical and diffusive equilibrium had been reached at this point.

The chamber pressure was then reduced to ambient levels (1 bar) by rapidly venting the chamber to the outside. The chamber was then immediately repressurized to 3 bar. This depressurization and repressurization cycle was completed in about 5 seconds, which is fast enough to make gas diffusion in and out of the bubble negligible. After completing this first cycle, another set of images was acquired in all three planes consecutively over a time span of approximately 35 minutes. After imaging, the pressure cycle was repeated, down to 1 bar and immediately back up to 3 bar, followed by another round of imaging. This process was repeated three times in total. Finally, the pressure was reduced to ambient pressure and the sample reimaged in all three planes one last time.

2.2.5 Bubble size determination

A custom MATLAB script was used to determine the size of the bubbles from the MRI scans. For each two-dimensional image in the stack that contains a bubble, as shown for a representative bubble in Fig. 2.1A, the average signal of the surrounding white matter is subtracted. Then, the dark pixels inside the bubble that are more than one standard deviation of the background noise below the white-matter background are extracted. We refine the two-dimensional shape of the bubble then by filling any holes in the image and discarding pixels that have less than four nearest neighbors in the bubble. A representative result is shown in Fig. 2.1B. This results in a slight undercount of the bubble area, and consequently volume, that is worse for small bubbles than for larger ones. The code is freely available [56].

The stacks of the bubble images in the three anatomic planes are then used to determine the convex hull of the bubble from a combination of all the images. Alignment of the three stacks is accomplished by minimizing the surface area of this convex hull. The result is shown in Fig. 2.1C. Finally, the volume of the bubble is computed from the aligned stacks. From a systematic variation of the image analysis parameters, we estimate that the volume determination is accurate to within 5%.

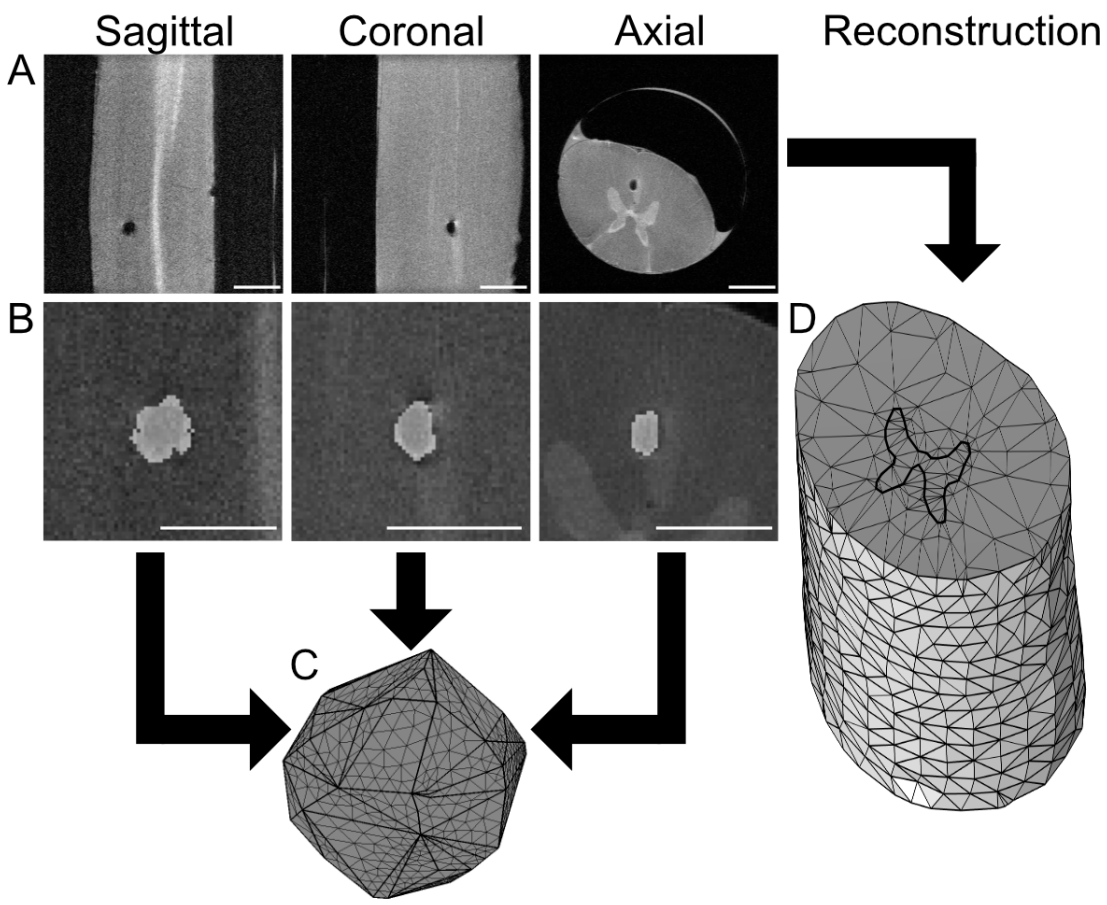

Figure 2.1: Reconstruction of the three-dimensional shape of a gas bubble from stacks of MR images in the three anatomical planes. (A) shows sample image slices of a bubble in the spinal cord in the sagittal, coronal, and axial planes, respectively. (B) shows the same slices after image processing to extract the bubble, and (C) shows the three-dimensional reconstruction of the bubble shape from the full stacks of these slices, and (D) shows the reconstruction of the surrounding spinal cord from an axial image stack. (A) scale bar = 5 mm (B) scale bar = 2.5 mm

2.2.6 Histopathology

To verify the existence of a gas bubble in the tissue, one sample was examined by means of histopathology. After the MRI scan, the axial location of the bubble as revealed in the image was marked with a fiduciary marker on the outside of the spinal cord. The tissue was fixed in 10% neutral-buffered formalin and then dehydrated in sucrose solution. The sample was sectioned on a cryo-microtome, stained with hematoxylin and eosin, and imaged with a

light microscope following routine procedures.

2.2.7 Geometric Models

We used COMSOL MULTIPHYSICS v6.1 to simulate the stress in the spinal cord tissue during bubble expansion through finite-element modeling. The model combines tissue mechanics with gas transport in a multiphysics approach, solving a mechanical model with nonlinear geometry for the tissue simultaneously with a diffusion-convection model for gas transport. The starting point is a geometric model of the spinal cord tissue that is constructed from our MRI image stacks using a custom MATLAB script. The gray matter consists of 1409 domain elements with 509 vertex elements, while the white matter comprises 4993 domain elements with 1487 vertex elements. This complex is shown in Fig. 2.1D.

The shape of the equilibrated bubble at 3 bars that was determined from the MRI scans as previously described in Fig. 2.1B is inserted as a void at the observed location. The surface of the embedded bubble adds another 146 vertex elements to the model. This domain is shown in Fig. 2.1C.

2.2.8 Initial and Boundary Conditions

We apply mechanical boundary conditions to the external surfaces of the tissue model such that an external gas pressure is applied to the outside of the sample. The external pressure also sets the boundary conditions for the dissolved gas concentration at the external surfaces of the tissue in accordance with Henry's law.

At the interface between the bubble and the tissue, the pressure inside the bubble pushes back against the tissue-bubble boundary. Initially, we assume after the one-day equilibration period at 3 bar, the pressure in the bubble equals the outside gas pressure. As the simulation progresses, the pressure inside the bubble is related to its gas content through the ideal gas law under isothermal conditions. As such, when the external pressure is reduced during

simulated decompression, the bubble is allowed to expand until a new mechanical equilibrium is reached. The gas concentration at the tissue-bubble boundary is again governed by Henry's law. As the simulation progresses and diffusion in the tissue leads to a concentration gradient at the tissue-bubble boundary, the flux in and out of the bubble is computed, which in turn changes the amount of gas and therefore pressure inside the bubble.

2.2.9 Material Model

For our tissue model, we assume a simple linear elastic model for both gray and white matter. Each tissue forms a distinct domain with different material parameters, which were taken from [1] and are shown in Table 2.1 below. Since the bubble is modeled as a void within the spinal cord, it does not have any associated material parameters.

For the tissue mechanics, we assume quasistatic behavior, as inertial forces and stresses related to the deformation of the tissue are negligibly small compared to the forces and stresses that are associated with changes in the external gas pressure or internal bubble pressure. Consequently, our model solves the time-independent Newton's second law equilibrium condition for the tissue. Geometric nonlinearities in the tissue response were computed at every step [57] to account for comparatively large strains in the deformed tissue near the bubble. All stresses that are reported in this article throughout are calculated as von Mises stresses.

For the gas diffusion, we assume the nitrogen-water diffusion coefficient for diffusion in both the white matter and the gray matter. These values are listed in Table 2.1.

	Density (kg/m^3)	Poisson Ratio	Young's Modulus (Pa)	Diffusion Coefficient (cm^2/s)
Gray Matter	1045	0.4	1.66E6	2E-5
White Matter	1041	0.42	9.42E5	2E-5

Table 2.1: Material parameters for gray and white matter used for the finite-element model, from [1] and [2].

2.3 Results

2.3.1 Bubble Formation

The spinal cord samples were subjected to 7 bar for 48 hours to ensure nitrogen saturation in the tissue and then depressurized to 3 bar and equilibrated after 24 hours, as described above, and shown in Fig. 2.2A. Bubble formation was visible in only six of ∼50 samples despite the rather aggressive pressurization / de-pressurization protocol that yields many more bubbles in agarose or gelatin phantom tissues, both in control experiments performed by us and previously reported in the literature [58]. Of those six bubbles, three formed at the edge of the sample and were physically connected to the outside. We excluded these from our analysis. All observed bubbles were formed in the white matter.

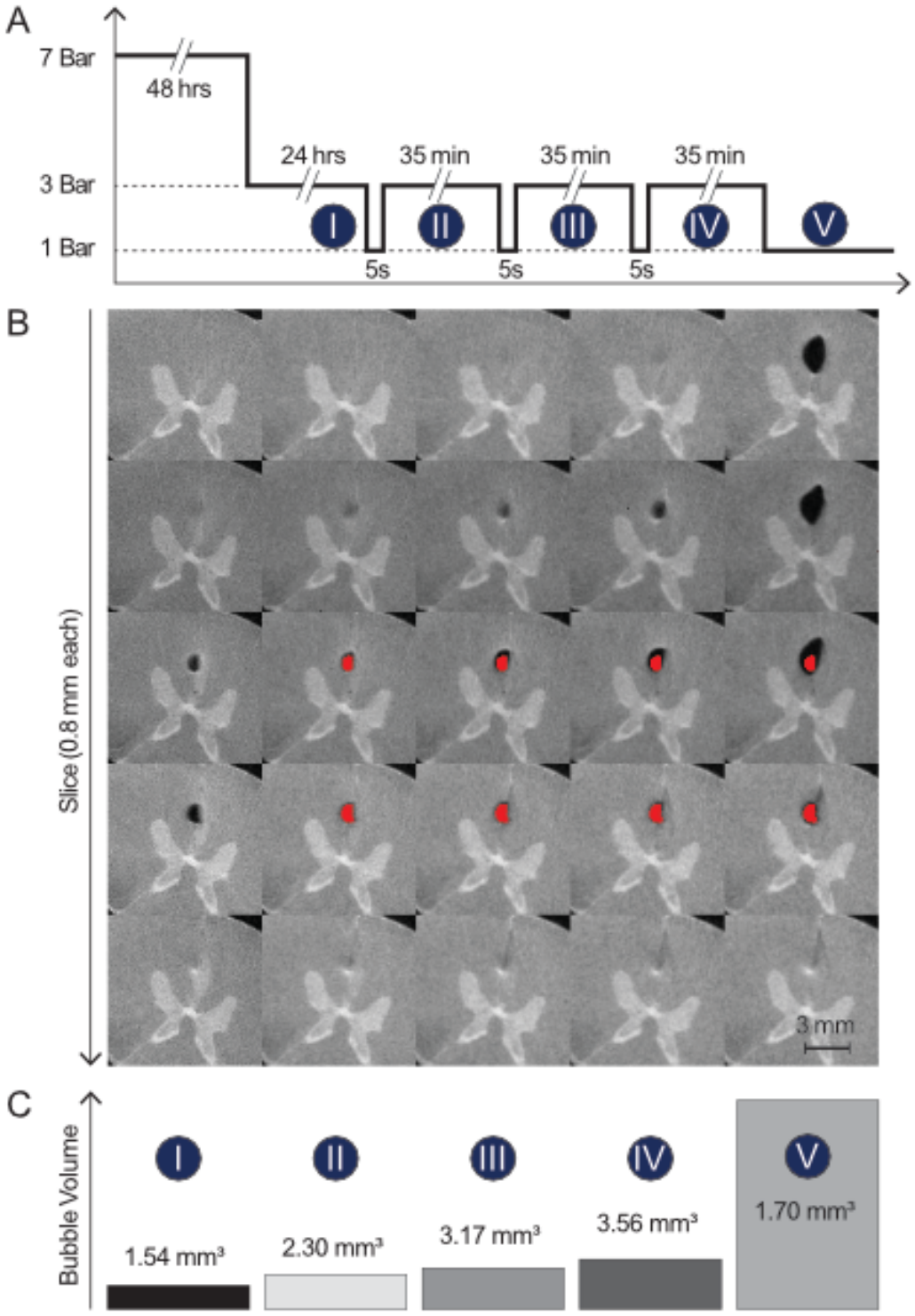

Figure 2.2: An example for one bubble growth is shown. (A) The pressure cycle is shown that is applied to all samples. Samples were imaged at points I, II, III, IV, and V. (B) Axial MRI scans show bubble growth for each pressure cycle. The leftmost frame indicates the equilibrated bubble and is overlaid in subsequent frames as a reference (red). (C) The bubble volume is quantified and shows a clear increase in volume for each pressure cycle.

2.3.2 Damage from Pressure Cycling

After the initial bubbles have formed and reached equilibrium, the external pressure is cycled as described above to probe the mechanical response of the surrounding tissue to pressure-induced bubble expansion and recompression. We observe that each of these pressure cycles results in an increase in bubble volume (Fig. 2.2C-2.2D).

From the repeated MRI scans in the three anatomical planes, the bubble volume is determined before and after each decompression-recompression cycle (Fig. 2.3). In the first cycle, the bubbles grew 37.2±3.1% (average ± standard error of the mean) relative to the initial cycle. Each subsequent cycle saw less bubble growth, 13.6 ± 5.8% and 9.56 ± 0.78% respectively, for cycles 2 and 3, relative to their previous cycle. The increase in bubble volume per the same pressure cycles indicates irreversible deformation is occurring in the spinal cord. Each successive increase in bubble volume is smaller and smaller and can be attributed to nonlinear and viscoelastic effects of the spinal cord. Each bubble experiences significant growth upon final decompression, (640 ± 150%) relative to the initial, equilibrated bubble and (313 ± 29%) compared to the bubble after the last recompression cycle. Unlike the growth during the recompression cycles, where the external pressure is returned to the pre-decompression value, the final expansion can largely be explained by a simple volumetric gas expansion following Boyle's Law. To rule out the gas diffusion into the bubble from incomplete equilibration, three control bubbles scanned consecutively without pressure cycling. They showed an apparent average growth of 3.71±2.45%.

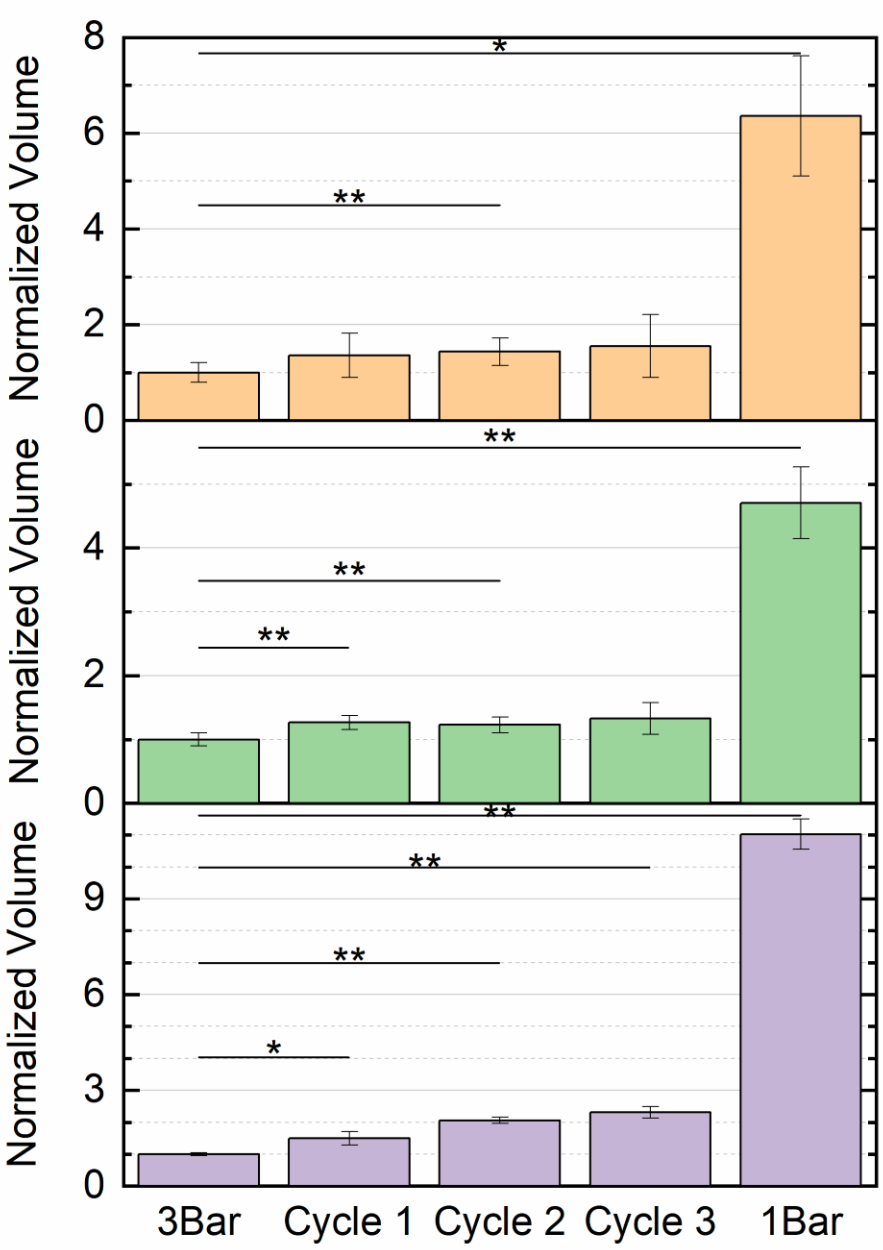

Figure 2.3: The normalized volume for 3 bubbles is shown. Every bubble grew in volume with each consecutive cycle. Error bars represent the confidence interval from the combined ratios of the standard error of the mean of averaged bubble volumes divided by their means. *$p<0.05$; **$p<0.01$.

2.3.3 Histopathology

For one sample, we confirmed the location and nature of the gas bubble in the tissue by means of histopathlogy. Fig. 2.4 shows the bubble in the expected location, but slightly

smaller than what is seen in the MR images. We attribute this minor discrepancy to shrinkage of the bubble during the lengthy fixation process.

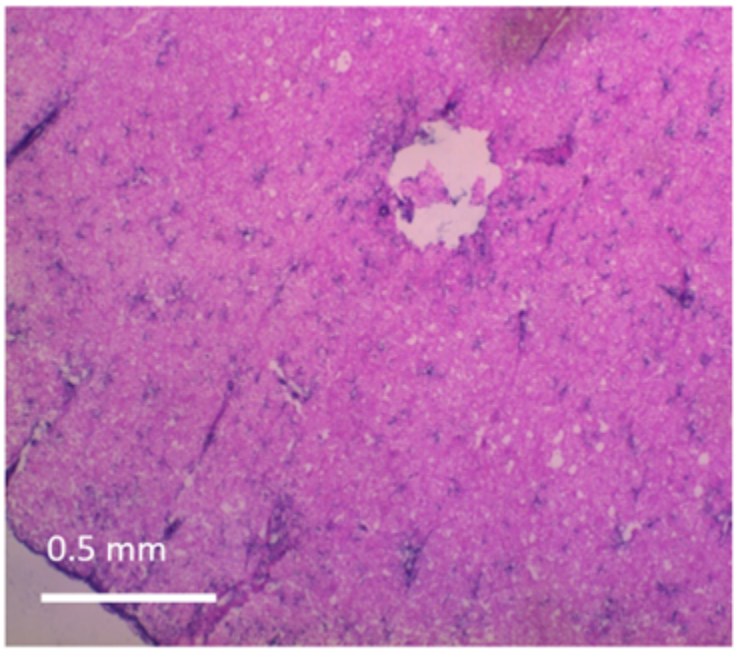

Figure 2.4: Histologic image (H&E) of a bubble in the spinal cord, taken from a fully decompressed sample after MR imaging. The bubble is located in the same place as seen in the MRI images.

2.3.4 Finite-Element Modeling

The model bubble experienced significant stress when subjected to decompression by rapidly changing the external pressure from 3 bars to 1 bar. Fig. 2.5A shows the average surface stress of the bubble as a function of time during a decompression / recompression cycle. The average stress of 125 kPa at the edge of the bubble during decompression significantly exceeds the white matter tensile strength of 61.3 kPa [1].

A further examination of the surface stress of the bubble after decompression yields a 2-D cross section of the stress as shown in Fig. 2.5C. The stress is localized near the surface of the bubble with higher stresses near coarser edges. A vertical 1-D cross section through the bubble further confirms the strong localization of the stress near the surface of the bubble (Fig. 2.5D). Stress exceeding the tissue tensile strength did not extend beyond 15% of the

bubble diameter (shaded).

While the model tissue was decompressed by lowering the external pressure, the pressure inside the bubble decreased from 3 bars to 2.38 bars (Fig. 2.5B). We note this internal pressure is considerably higher than the external pressure of 1 bars after decompression. Correspondingly, the bubble increased in volume only by approximately 27% (Fig. 2.5B) instead of threefold as one might expect from Boyle's Law had the bubble pressure dropped to 1 bar. This substantial excess internal pressure in the bubble is balanced by the mechanical stress in the surrounding tissue. Altogether, the magnitude of the stress in the tissue immediately surrounding the bubble suggests that tissue failure in white matter is the most likely explanation of our observations.

Because gas diffusion is a slow process, the bubble does not reach equilibrium with its surroundings during the very short decompression cycle and gas from the white matter flows into the bubble. However, the overall effect from this gas inflow is negligibly small and amounted to an increase in the average surface stress of 0.08 kPa and a 0.000 15 mm^3 (0.0078%) increase in bubble volume during the entire decompression cycle. This validates our assumption that we can attribute the experimentally observed bubble expansion to a purely mechanical tissue response, while contributions from gas diffusion can be disregarded on our time scale.

When the external pressure is restored to its pre-decompression value, the bubble volume and the stress in the tissue revert to their original values as shown in Fig. 2.5A-2.5B, again with negligible effects in gas diffusion, validating our simulations using the assumption of an elastic tissue model. This is, however, in contradiction to the incremental growth observed in our experiments and contributes to the mounting evidence suggesting that a reversible elastic response is insufficient in capturing the intricate mechanics associated with bubble growth during decompression, as discussed in more detail below.

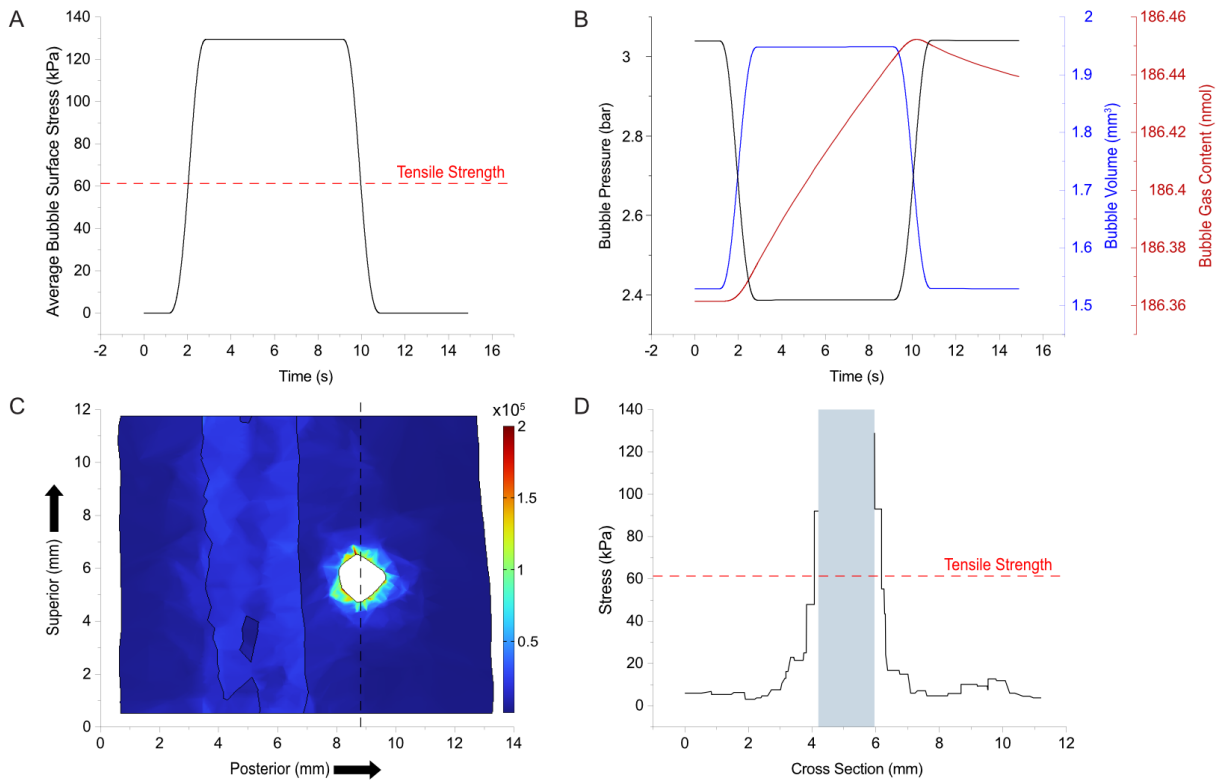

Figure 2.5: The FEM model was decompressed for 2 bars. (A) The average bubble surface stress exceeded the tensile strength of the surrounding white matter (red dashed line). (B) The decrease in external pressure caused the bubble to expand and decreased the internal bubble pressure. Gas flowed into the bubble to reach a new equilibrium but had very little effect on stress and volume at these time scales. (C) A 2D cross section at 5.11 s shows high stress at the bubble's edges. The vertical cross section (black dashed line) reveals (D) exponential stress exceeding the surrounding white matter tensile strength (red dashed line) near the boundary of the bubble (shaded).

2.3.5 Discussion

Neurological DCS poses significant clinical challenges, and although bubbles are recognized as the main contributor to SC-DCS pathogenesis, the exact mechanisms by which they cause the clinically observed symptoms remain elusive. Generally accepted mechanisms through which growing bubbles cause damage to the spinal cord involve the blockage of blood flow by the bubbles and, hence, an infarction of the spinal cord tissue [29, 53, 54] or complement activation at the tissue-air interface of the bubbles [59].

Here, we present evidence for a different mechanism by which a growing bubble can cause neurologic damage: by mechanically tearing or viscoelastically deforming the tissue adjacent to the gas bubble irreversibly, which effectively results in a small traumatic spinal cord injury. To reach this conclusion, we mechanically probed the response of ex-vivo bovine spinal cord tissue to an expanding gas bubble by externally pressure cycling it. We observed an irreversible incremental growth of the bubble during each rapid decompression and recompression cycle. This behavior is inconsistent with the notion that the bubble is lodged in a blood vessel and responds elastically to pressure changes by expanding in the vessel without mechanically breaching the surrounding endothelium. Instead, we see that the expanding bubble creates a space for itself that it can expands into by irreversibly deforming the surroundings of the bubble.

The measured bubble volumes from our experiments allow us to get a sense of the forces that the growing bubble exerts on its surroundings through finite-element modeling. When we use a linear elastic tissue model for the spinal cord to simulate our pressure cycling experiments, the model predicts stresses in the tissue that exceed the tensile strength for nerve tissue more than threefold in an area that is highly localized around the bubble. This confirms that the forces associated with a growing gas bubble can indeed be large enough to cause permanent mechanical damage. This validates not only our experimental findings but also tracks the histological observations by [20] in decompressed dogs, where they found cell debris in proximity to the bubbles in the spinal cord.

In clinical practice, the administration of normobaric oxygen followed by hyperbaric recompression treatment is the gold standard for treating DCS. Variations of this protocol have been in use for over a century [60]. The purpose of this treatment is to shrink the bubble and reoxygenate the tissue. Yet the success of this treatment is highly variable and the factors that lead to complete resolution are poorly understood. For SC-DCS, incomplete resolution of symptoms or even total failure of the treatment [61] is reported in roughly one-third of all cases, with the severity of the initial symptoms as the primary predictor of success or

failure [62]. Often, the persistence of bubbles after hyperbaric treatment is observed [63], and higher risk of DCS in future diving is reported [64].

Our findings can potentially provide an insight into the high variability of treatment success and some of the other unexplained phenomenology. Damage from bubbles that tear the surrounding tissue is likely more severe and persistent that damage from bubbles that are just ischemic in nature. Therefore, the presence of severe symptoms in the early presentation may indicate a traumatic injury, which in turn leads to longer-lasting damage, Second, the traumatic nature of the injury in these cases may lead to the local formation of scar tissue. That can predispose this location to the future formation of large bubbles in that place, because a weakened gap structure may already exist into which a future bubble can readily expand. This would naturally explain the not infrequent occurrence of sequelae of SC-DCS on innocuous dives even months after the initial treatment and resolution of symptoms.

2.3.6 Conclusion

This study contributes to our understanding of SC-DCS by demonstrating growing decompression gas bubbles cause the direct mechanical damage to ex vivo bovine spinal cord tissue that is not adequately described by a reversible elastic response of the surrounding tissue. These findings emphasize that it is important to consider SC-DCS to be a multifaceted condition that may require a comprehensive approach in its treatment that goes beyond shrinking the offending gas bubble and reoxygenating tissue, but also addresses the traumatic nature of the injury in its management.

CHAPTER 3

A Tissue Mechanics-Gas Diffusion Model for Decompression Sickness

In this chapter, we present a comprehensive model that couples tissue mechanics and gas diffusion to provide a more accurate understanding of bubble mechanics during decompression. This model was developed as a means to escape the use of empirical data in the development of current models. Our findings suggest that tissue elasticity plays a critical role in moderating bubble stress, especially in different pressure regimes. We also observe that small bubbles are governed by diffusion effects, while larger bubbles are dominated by tissue mechanics. This study demonstrates that both decompression and recompression can induce stresses that exceed tissue tensile strength. Additionally, we propose that there exists a bubble size where the interaction between gas flux and tissue mechanics results in maximum stress. Further research is needed to explore the effects of tissue-specific responses and the timing of recompression therapy.

3.1 Introduction

A century of research has determined bubble formation plays a significant role in decompression sickness, which is brought about by a decrease in ambient pressure. However, the pathophysiology of DCS, which includes milder Type 1 symptoms such as rashes [65] and more severe Type 2 symptoms such as paralysis [65], is not well-understood [66]. Since the

onset of DCS was first recognized, many scientists have developed decompression models to minimize DCS incidence.

A common feature of all these models is the principle of minimizing the tissue supersaturation during decompression, which fundamentally aims to reduce bubble formation [46, 67, 68]. The data that has been used to create tables has been a result of years of empirical approaches, where tables were refined for specific diving practices and for specific diving populations[48] and so, may not always work for every diver. This is especially true as DCS seems to have an inter-individual variability [48, 49]. As a result, divers often choose their acceptable level of DCS risk to formulate their targeted decompression rate modern decompression tables [69, 49].

In this article, the primary objective of this study is to provide a more accurate and detailed understanding of the factors influencing bubble growth and dissolution by presenting a comprehensive model that couples tissue mechanics and gas diffusion. Here, we extend the analysis of the model presented in Chapter 2. We examine the importance of tissue mechanics, the effects of decompression time, and the dynamic behavior dependence on bubble seed size. Our analysis suggests tissue elasticity plays different roles at different pressures, recompression can exceed tissue tensile strength comparable to decompression, and small bubbles are dominated by diffusion effects while large bubbles are dominated by tissue mechanics. This model aims to enhance decompression protocols, reduce DCS incidence, and improve safety and treatment outcomes for divers and astronauts.

3.2 Methods

3.2.1 Model Geometry

The same model was used as described in Chapter 2 for all results reported herein except when assessing the stress effects as a function of bubble size. For this analysis, a spherical bubble with 428 surface vertices was employed for all bubble sizes. The mesh face area

changed accordingly to maintain a consistent number of vertices and triangles.

3.2.2 Model Equilibrium Equations

For completeness, the physics employed in this COMSOL model are the Solid Mechanics (SM) and Transport of Diluted Species (TDS) modules. The SM module solves the time-independent Newton's second law, written as

$$0 = f_V + \nabla \cdot \sigma \tag{3.1}$$

where f_V is the body force per unit volume and σ is a stress tensor representing the internal stresses in the material. For gas diffusion, we can simplify our equation because we are only considering one gaseous species in our system. Thus, the equation of interest for gas diffusion is

$$\frac{\partial c}{\partial t} + \nabla \cdot (-D\nabla c) = R \tag{3.2}$$

where c is the gas concentration, t is time, D is the diffusion coefficient, and R is a reaction rate that described the addition or removal of gas in the system. For further discussion of model assumptions, see the Material Model section in Chapter 2.

3.2.3 Model Equilibrium Equations

The initial and boundary conditions are consistent with those described in Chapter 2. For the sake of completeness, we present them in equation form here. We apply a changing hydrostatic pressure, P_h, to all external boundaries of the spinal cord model. This external pressure sets the boundary conditions for the dissolved gas concentration, c, at the spinal cord external surfaces, in accordance with Henry's law, which is expressed as

$$c = P_h H_s \tag{3.3}$$

where H_s is Henry's constant $6.36\times10^{-6}\text{mol}\,\text{Pa}^{-1}\,\text{m}^{-3}$ [70].

The mechanical equilibrium of the bubble is balanced by three pressures: the gas pressure inside the bubble pushing outwards, P_b, the ambient pressure on the spinal cord, P_h, and a pressure term that combines bubble surface tension and tissue deformation pressure dependent on tissue material parameters, P_t [8]. Additionally, we assume the bubble behaves as an ideal gas, and thus, the pressure of the bubble can be expressed as

$$P_b = P_h + P_t = c_b RT \tag{3.4}$$

where R is the universal gas constant, T is room temperature, and c_b is the gas concentration in the bubble. The gas concentration at the bubble-tissue interface is also set by Henry's law, as in Eq.3.3, with the corresponding bubble pressure in place of the hydrostatic pressure. This equation shows a coupling between the concentration set by Henry's law and tissue mechanics that is specific for different ambient pressures.

3.2.4 Accounting for Different Frames of References

The SM module is solved in the Lagrangian frame of reference in which the stresses and strains are computed in a coordinate system that moves with the material [71]. However, the TDS module is solved in the Eulerian frame of reference in which the concentrations are solved in a fixed coordinate system [71]. The result is that the TDS module will not consider changes to the model geometry, such as volume and boundary changes. Additionally, neither can easily accommodate the other given our problem of interest. It is therefore necessary to develop a set of equations to couple these physics. We thus consider three conditions:

(1) Consider an enclosed volume with a fixed quantity of gas with permeable boundaries. If the system is out of equilibrium, gas will move across its boundaries to reach equilibrium. Correspondingly, the enclosed gas concentration must change accordingly.

(2) Consider the same system as in (1), but with non-permeable boundaries. As the

walls expand, the enclosed gas concentration decreases inversely proportional to the volume expansion.

(3) Consider the same system as in (2). As the walls expand, gas nearest the boundary will move faster in the direction of the moving boundaries to maintain an equally distributed enclosed gas when compared to gas located at the center of the system.

Note, conditions (1) and (2) are a change in concentration in time and are therefore a change in the bulk domain concentration. However, condition (3) is a change in the gas diffusion coefficient and determines the local concentration. We can mimic conditions (1) and (2) in COMSOL by implementing an equivalent chemical reaction, taking care of which gas content is accounted for in each domain. For domains defined with the TDS module, such as the gray and white matter, condition (1) is automatically accounted for. Thus, the general equivalent chemical reaction R_g, that is evaluated at every step, takes the form

$$R_g = \frac{n_t}{t_s}\left(\frac{1}{V_d} - \frac{1}{V_{dp}}\right) \tag{3.5}$$

where n_t is the net number of moles moving across the domain of interest, V_d is the domain current volume, V_{dp} is the previous step domain volume, and t_s is the timestep. A similar expression is used for the bubble, but we must also account for condition (2) because it is not defined by the TDS module. Additionally, as we are tracking the bubble concentration separately, we need a total change in concentration Δc_b. This can be done by integrating the equivalent chemical reaction for the bubble R_b with respect to time,

$$\Delta c_b = \int_0^t R_b\, dt = \int_0^t \frac{1}{t_s}\left(\frac{n_{b0} + n_b}{V_b} - \frac{n_{b0} + n_{bp}}{V_{bp}}\right) dt \tag{3.6}$$

where n_{b0} is the initial bubble gas content, n_b is the current gas content moving across the boundary, n_{bp} is the previous mol count moving across the boundary, V_b is the current bubble volume, and V_{bp} is the previous bubble volume. The change in concentration described by Eqns. 3.5-3.6 assumes an equal expansion in all directions. An additional coupling must be

made to change the rate of diffusion when the domain walls move and thus satisfy condition (3). This can be done by scaling the diffusion coefficient as

$$D = \begin{pmatrix} D_0\lambda_1^2 & 0 & 0 \\ 0 & D_0\lambda_2^2 & 0 \\ 0 & 0 & D_0\lambda_3^2 \end{pmatrix}$$

where D_0 is the same the diffusion coefficient in Table 2.1 for an undeformed geometry, and $\lambda_1, \lambda_2, \lambda_3$ are the principal stretch ratios calculated by the SM module. Equations 3.5 and 3.6 depend on the accurate transfer of gas content moving across any boundary at each step. This is not defined in COMSOL and so, the expression for any mol count moving across any boundary, n_b, can be calculated by the expression

$$n_b = \int_0^t S_A(\phi_c \cdot \hat{n_b})\, dt \tag{3.7}$$

where S_A is the surface area of the boundary, ϕ_c is the concentration flux, and $\hat{n_b}$ is the surface normal.

3.3 Results

3.3.1 Effect of Different Decompression Profiles

We decompressed the same model using two different pressure profiles, specifically 3:1 and 1:1/3 absolute atmospheres (ATA) decompression ratios, to understand the stress impact on the surrounding tissues (Fig. 3.1A). These profiles were chosen to compare a typical spacewalk decompression profile [72] while maintaining the same bubble volume expansion under the assumption that bubbles behave in accordance with Boyle's Law. The 3:1 ATA profile corresponded with a normalized growth of 27% while the 1:1/3 ATA decompression profile corresponded with a normalized bubble growth volume of 11%, a moderate difference

of 16%. Upon decompression, both models returned to their original equilibrium.

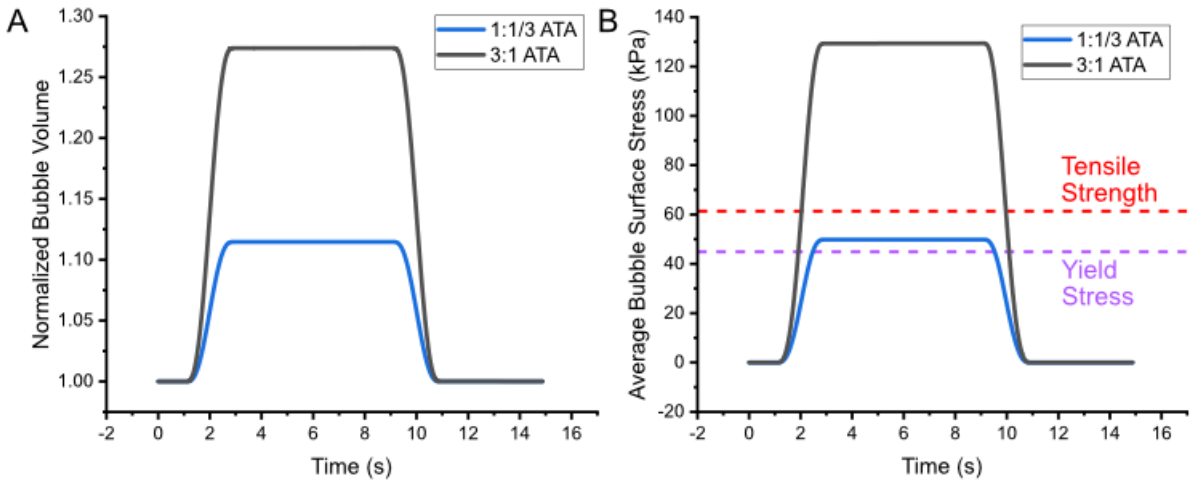

Figure 3.1: Average surface stress for two different decompression profiles of the same ratio is shown. The decompression profile of 3:1 ATA causes a significantly higher stress response compared to the 1:1/3 ATA decompression profile.

More interestingly, the bubble surface experienced significantly higher stress following the 3:1 ATA decompression profile compared to the 1:1/3 ATA decompression profile (Fig. 3.1B). Specifically, the 3:1 ATA profile resulted in a peak surface stress of 130 kPa while the 1:1/3 ATA profile resulted in a peak surface stress of 50 kPa. Although each decompression/compression cycle was a threefold change, the 1:1/3 ATA did not exceed the surrounding tissue tensile strength, but did exceed the surrounding tissue yield stress with our material parameters. However, experimental evidence has shown the tissue yield stress is variable between spinal cord samples [1]. We emphasize, for our different material parameters, the average bubble surface stress could remain below the yield stress. While neither was allowed to equilibrate during decompression, the average surface stress and volume change were significantly different.

3.3.2 Effect of time on bubble stress

We extended the model to simulate 48 hours using the same decompression/compression rate (Fig. 3.2A). The model was maintained in the decompressed state for 24 hours and in

the recompressed state for another 24 hours. The peak stress in the decompressed state was 134 kPa, 20 min after decompression. This peak stress corresponded with a 24% increase in volume change relative to the original volume (Fig. 3.2B). Similarly, the peak stress in the recompressed state was 112 kPa, 15 min after initial recompression. This peak stress corresponded with a total volume change of 32%, but it represented a 22% change relative to the original volume. Both decompression and recompression peak stresses exceeded the surrounding tissue tensile strength of 61.3 kPa.

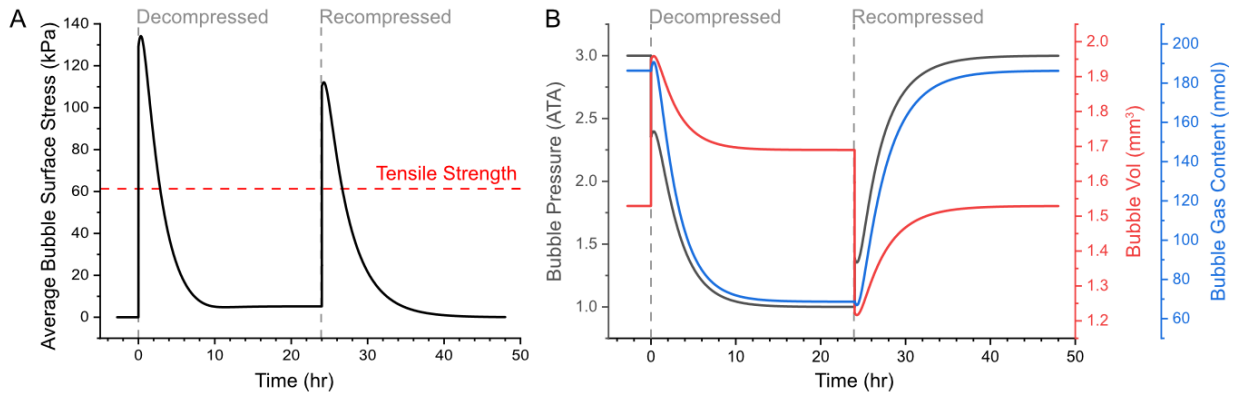

Figure 3.2: (A) The average surface stress of the bubble peaks beyond the tensile strength at decompression and at recompression. (B) At decompression, the bubble expands, resulting in a decrease in bubble pressure. Gas flows into the bubble via Henry's law until the concentration in the spinal cord significantly decreases, causing gas to flow out of the bubble until equilibrium is reached. The reverse occurs during recompression.

A closer examination of the decompressed state revealed the internal pressure of the bubble matched the reduced external pressure of 1.001 ATA, in 18.5 hours (Fig. 3.2B). However, it's important to note that the average surface stress of the bubble never returns to zero stress during the decompressed state and instead equilibrates to 5kPa. This can be attributed to a corresponding volume being 10% larger than its original volume. Upon recompression, the bubble nearly returns to its original equilibrium within 24 hours. The time to return to equilibrium is likely longer than in a native spinal cord, as we are not taking into account the process of gas removal from the blood circulation.

3.3.3 Seed Bubble Size

The model was decompressed using the 3:1 ATM pressure profile for a wide range of bubble diameters spanning from 5 µm to 3065 µm (Fig 3). This range was chosen to examine relevant microbubbles observed in reported data [24, 73, 74] and to include larger diameters discussed in Chapters 2 and 4.

The bubble pressure was reported for the duration of the simulation (Fig. 3.3A). Small bubbles appear to quickly equilibrate after decompression while large bubbles do not have a strong diffusion dependence after decompression. However, intermediate bubbles exhibit large changes in initial pressure and equilibrate quickly after decompression. This behavior suggests a size transition in which gas mechanics is more important than tissue mechanics and vice versa.

To understand how this behavior would impact damage to the spinal cord, we examined the average surface stress of the bubble (Fig. 3.3B). It quickly became apparent a wide range of behavior can be observed, with small bubbles reaching a maximum stress faster than others with varying ranges of stress. As diffusion is the main factor after initial decompression, the models at decompression (t=2.9s to t=9.08s) were fitted with the function

$$\sigma_A = Je^{-Kt} + L \tag{3.8}$$

where σ_A is the average surface stress. The fit parameter J corresponds to the initial stress, K is the stress rate of change, and L as the apparent stress equilibrium at decompression (Fig. 3.3C). Ideally, parameter J would be near zero as decompression occurs rapidly near the origin, and this is reflected in diameters larger than 20 µm. Parameter K and L are dependent on the rate of diffusion, but in general, they increase as diameter decreases.

The parameter K is of interest as it only reflects the impact of diffusion on tissue stress relaxation. We invert this variable to determine a 3D random walk diffusion timescale, Δt¸ and calculate the diffusion step $d_s = \sqrt{6D\Delta t}$. We see, in general, the average step diffusion

increases linearly with an increase in bubble diameter (Fig. 3.3D). However, intermediate bubbles (diameters near 100 µm) have an increase in step length. These bubbles are the largest prior to an observed increase in stress seen in smaller bubbles.

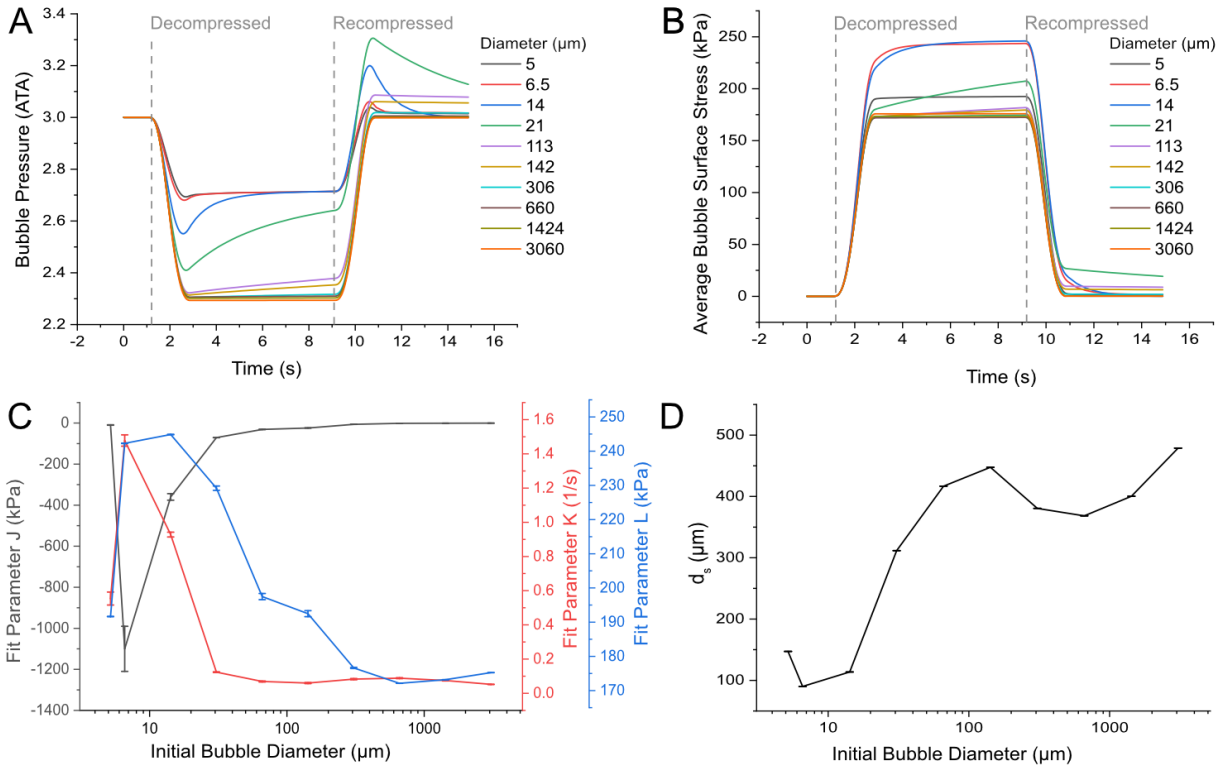

Figure 3.3: (A) The bubble pressure for different bubble sizes. The initial drop in bubble pressure decreases as bubble size decreases. (B) The average surface stress of the bubble increases for very small bubbles. (C) The average surface stress during decompression was fit with Eq. 3.8 for all bubble diameters. Parameter K can be related to random walk diffusion, indicated in the text, where (D) we see a linear dependence between diffusion step size and bubble diameters. There is an increase in step length at ∼100 µm bubble diameter.

To better understand the complexities observed in the complete model across spatial scales, two validation tests were performed. The first series of simulations were performed where the gas diffusion mechanics was disabled (Fig. 3.4A-C). Here, we fixed the bubble pressure to 3 ATA and decreased the external pressure, causing the bubble to expand. The majority of the bubbles, diameters between 14-660 µm, had little variation in stress 305.9±1.4 kPa (average ± standard deviation) (Fig. 3.4A). However, larger bubbles experienced a

peak average stress of 316.72 (3.5% greater, Welch's T-test =164723) while smaller bubbles experienced significantly lower stress, 236.4 kPa (22.7% less, Welch's T-test =215645). Both large and small bubbles are significantly different and can be explained due to the geometry of the model. Large bubbles, experienced greater stress as they approached the boundaries of the gray matter (Fig. 3.4B). Smaller bubbles retreated from all boundaries and are likely sensitive to local strain and stress gradients.

A second series of simulations were performed where the bubble pressure was decreased at the same rate and target as the external pressure (Fig. 3.4D-F). However, while the pressure decreased, the bubble size was fixed and the concentration at the bubble boundary was still dictated by Henry's law. This test is designed to decrease the gas concentration at both the external and bubble boundaries, leaving only the effect of diffusion to be observed. As expected, the diffusion rate across the surface of the bubble increased for decreasing bubble size, spanning 5 orders of magnitude, and highlighting the dominant factor at play is the surface to volume ratio (Fig. 3.4D). After the initial peak, the diffusion rate decrased for larger bubbles and increased for smaller bubbles (Fig. 3.4E). To better understand this, a cross section of the smallest and largest bubble were taken at 100s, well into the second diffusion process, but understanding it is the dominant process after 12s (Fig. 3.4F). It is apparent the local gradient concentration is significantly (Welch's T-test = 1.3E16) steeper in the smaller bubble ($99\,000 \pm 7200\,\mathrm{mol\,m^{-2}}$) compared to the largest bubble ($997 \pm 34\,\mathrm{mol\,m^{-2}}$). It is evident the local concentration gradient, as shown in Eq. 3.2, drives the diffusion rate. Large bubbles quickly deplete the surrounding tissue concentration and as a result, the diffusion rate to the bubble is reduced. However, small bubbles do not deplete the surrounding tissue in a similar manner and thus, the surrounding tissue is able to sustain the diffusion rate for smaller bubbles. The combined independent effect of tissue and gas mechanics results in dynamic behavior seen in Fig. 3.4 with an apparent bubble diameter of about 100 µm that is sensitive to gas and tissue mechanics.

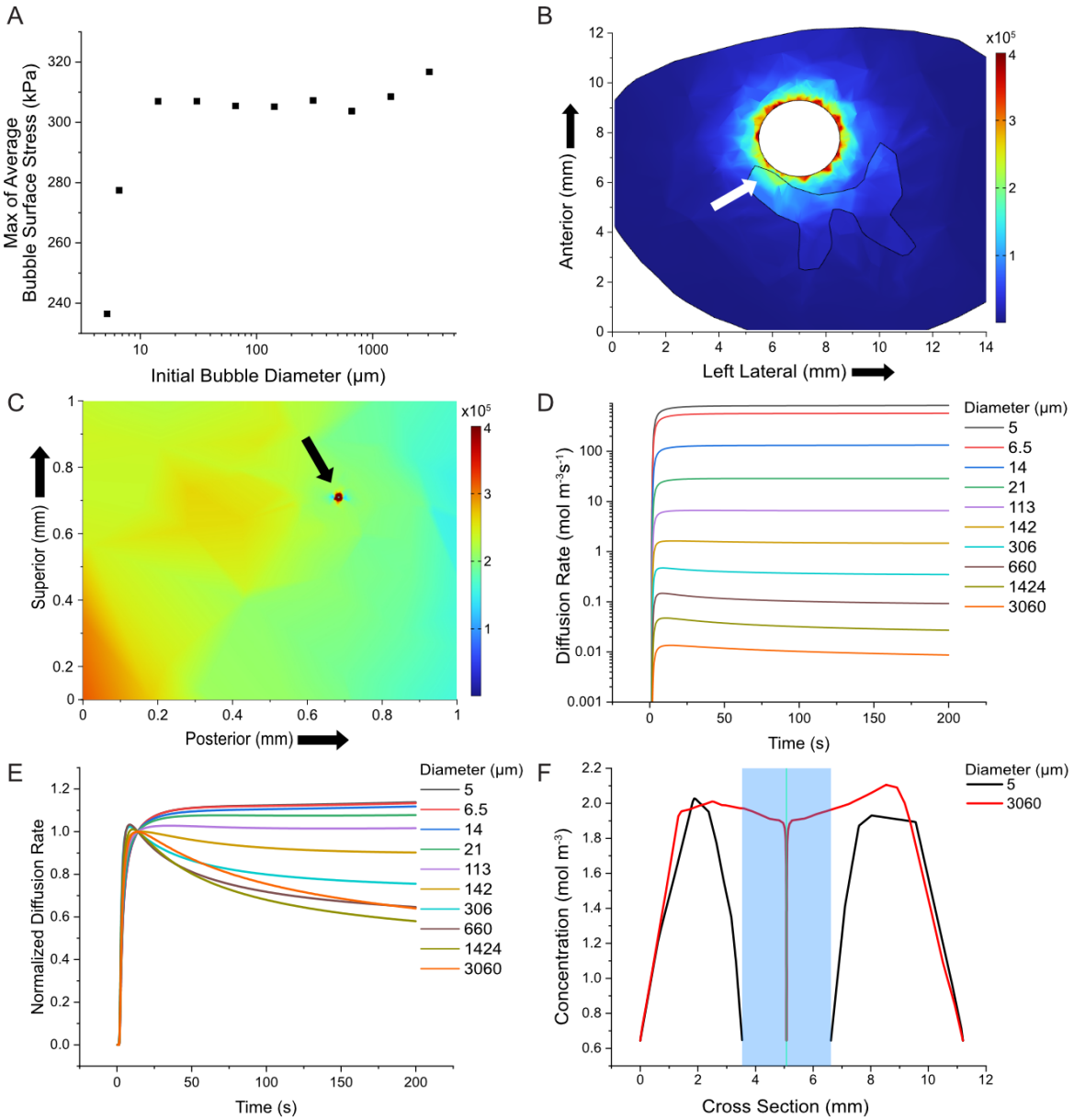

Figure 3.4: (A) The tissue mechanics validation tests revealed a decrease in stress at very small bubbles and an increase in stress with large bubbles. The increased surface stress for large bubbles can be explained by (B) the bubble interacting with the boundaries of the surrounding tissues (white arrow). (C) Small bubbles (black arrow) experienced lower average surface stress because of local stress gradients. (D) The gas mechanics validation tests revealed the initial diffusion rate is determined by the surface area to volume ratio of the embedded bubble. However, (E) the secondary diffusion rate depicted large bubbles decreasing in diffusion rate while small bubbles had an increase in diffusion rate. This is because (F) the local gradient concentration is significantly steeper with smaller bubbles than larger bubbles. The shaded regions show the bubble diameters.

3.4 Discussion

In Chapter 2, we presented the importance of tissue elasticity and the ability of the bubbles to exceed the surrounding tissue tensile strength. Here again, we present data on the importance of consideration of tissue elasticity and its effect to change the resulting average surface bubble stress when comparing 3:1 and 1:1/3 ATA decompression profiles. Previous tissular bubble models assumed the bubbles experienced the same pressure change with proportional volume changes [75]. Practically, this would assume the same stress would be experienced by a bubble in a 3:1 and 1:1/3 ATA as they share the same factor of 3 in pressure change. However, our model suggests a significant decrease in average surface stress for the 1:1/3 ATA decompression profile because of the effects of tissue elasticity. This may explain why astronauts, who undergo a 1:1/3 ATA decompression in preparation for spacewalks, experience a lower incidence rate for DCS [76] and are easier to treat [77] compared to divers [78].

In all figures presented in this article, the state of decompression always yielded an average stress significantly higher than the surrounding tissue tensile strength and yield stress. For this decompression profile and more extreme decompressions, this may explain the inadequacy of relieving neurological decompression symptoms upon recompression [33]. In addition to revealing irreversible decompression mechanisms, we also demonstrated the act of recompression can result in a similar average stress exceeding the tissue tensile strength. Although it is generally recommended to receive timely recompression therapy [42] because of better clinical outcome if treated within the first 12 hours of onset symptoms [79], other studies have shown delayed recompression treatment had no significant effect on the clinical outcome [33, 34, 80]. Our study therefore suggests there may be an optimal time for recompression. A more thorough investigation should be conducted to determine the latest time at which recompression should be performed and if different tissues result in different outcomes (i.e., Type 1 vs Type 2 DCS).

Investigating the effect of bubble size on the average surface stress, the dominating factor

in large bubbles is the change in external pressure whereas the main stress factor in small bubbles is dominated by diffusion. As such, there seems to exist a bubble diameter where the interaction of gas flux and tissue elasticity result in greater stresses than the smallest or largest bubbles. It should be noted, however, that this linear elastic model may be insufficient for proper bubble size analysis. It has been reported that, for scales transitioning from the micro to macro scale, models tend to underestimate stress because higher order terms in the linear elastic strain formulation are ignored [81]. A simple ratio of an internal constitutive length parameter to that of the characteristic length of the deformation approaching unity should consider strain densities in stress calculations [82]. In this context, this would be the ratio of the size of a neuron cell to the bubble diameter where unity is approached for bubble diameters of 20 µm [83]. If omitted, this may explain the waved parameter fits for very small bubbles shown in Fig. 3.3C [84]. A more thorough investigation should be conducted to determine the importance of strain densities at very small scales for decompression bubbles to accurately estimate bubble surface stress.

3.5 Future Direction

The model discussed in this chapter is meant to extend the analysis for the equilibrated bubble observed in the ex vivo bovine spinal cord tissue. However, this model can be modified to accurately mimic physiologically relevant conditions. In this model, we are only considering a nitrogen gas source and incorporating oxygen would make a significant change to the observed bubble mechanics. To account for this, we can incorporate the different partial pressures of different gases, as well as the water vapor pressure in the human body. This results in a pressure at the external boundary condition, equivalent to the alveolar pressure (P_A), given as

$$P_A = P_{N_2} + P_{H_20} + P_{O_2} \tag{3.9}$$

where P_{N_2} is the inspiration pressure from nitrogen, P_{O_2} is the inspiration pressure from oxygen, and P_{H_20} is the static water vapor pressure in the body of 0.062 atm [85]. The pressure inside the bubble is the same as Eq. 3.9 with the omission of the oxygen term, as decompression bubbles are composed of nitrogen [4]. Eq. 3.9 can also be moved to the boundary of the bubble to simulate bubbles circulating in the blood stream.

Secondly, we can incorporate accurate material models to replace our linear elastic model assumption. Most biological tissues exhibit large deformations, are nearly or completely incompressible, and nonhomogeneous [86]. This has led to a plethora of studies to examine the complex coupling of these behaviors under different loading conditions [87]. To that end, we are currently replacing the linear elastic material model with an incompressible hyperelastic Ogden material model. The equation form is

$$U = \frac{2\mu}{\alpha^2}(\lambda_1 + \lambda_2 + \lambda_3 - 3) + \frac{1}{D}(J-1)^2 \tag{3.10}$$

where U is the stress strain energy function effectively replacing σ in Eq. 3.1, α and μ are material parameters, $\lambda_1, \lambda_2, \lambda_3$ are the principal elastic stretch factors, J is the elastic volume ratio and equal to the product of all three principal stretch factors. The material parameters are taken from [88], a preferred source among spinal cord injury modeling [89], and summarized in Table 3.1.

	Density (kg/m^3)	α	μ (kPa)	D (MPa^{-1})
Gray Matter	1050	14.7	4.1	50.5
White Matter	1050	12.5	4	51.7

Table 3.1: Nearly incompressible Ogden material parameters for gray and white matter.

Additional tissue mechanics behavior, such as viscoplasticity and ratcheting can be added, but would require collection of experimental data. A comparison of tensile and compression strength should also be performed for proper decompression/recompression analysis.

The final component to be added for a physiologically accurate model is to incorporate the

exchange of dissolved gases with tissues. This extension would follow the original Haldane model with modifications made by Bühlmann, where the rate of gas exchange is driven by the nitrogen gas pressure gradient between the nitrogen gas breathed and the nitrogen gas in the tissues [49]. It is generally agreed that this behavior follows an exponential kinetic gas function of the form

$$P_T(t_E) = P_T(t_0) + [P_{N2} - P_I(t_0)][1 - e^{-ln(2)\frac{t_E}{t_{1/2}}}] \tag{3.11}$$

where P_T is the nitrogen gas in the tissue, t_0 is the initial exposure time to the change in inspiration pressure, t_E is the time of exposure at the changed inspirational pressure, $t_{1/2}$ is the half-life gas exchange rate specific for different tissues. However, this gas exchange pressure would need to be implemented into COMSOL using another chemical reaction, yet to be determined. Regardless, these implementation changes enable this model to develop new decompression profiles to minimize the incidence of DCS.

CHAPTER 4

Real-time Imaging of Decompression Gas Bubble Growth in the Spinal Cord of Live Rats

In this chapter, we present a method to observe the growth and resolution of decompression gas bubbles in the spinal cord of live rats in real-time using magnetic resonance imaging using a custom built pressure chamber. The system pressurizes and depressurizes rodents while inside an MRI scanner and monitors their respiratory rate, heart rate, and body temperature while providing gaseous anesthesia under pressure during experiments. This system can be extended to include various breathing gasses and variable pressure rates.

4.1 Introduction

Decompression sickness is generally thought to be caused by the formation of inert gas bubbles in the body that arise from a supersaturation of the tissue with gas on a rapid reduction in the ambient pressure [90]. Aural Doppler ultrasound and 2D echocardiography have long been used to monitor the formation of circulating decompression bubbles in large veins or the heart post dive [91]. However, although these circulating bubbles are present in virtually all cases that result in DCS, their presence alone does not reliably predict DCS symptoms, and even less so the development of SC-DCS [92]. For pathophysiological studies

of SC-DCS, it is, therefore, important to directly study the bubbles in the spinal cord itself instead of relying solely on readily observed circulating bubbles. Gas bubbles in the spinal cord are, up to now, only examined postmortem using pathology, which is rather limiting as it reveals no dynamic information, and it is fraught with artifacts from fixation and slicing that are often hard to distinguish from gas bubbles [29].

We demonstrate that it is possible to observe the formation of gas bubbles in deeper tissues directly in vivo using MRI. However, there are considerable technical challenges in combining the hyperbaric environment with MRI and maintaining anesthesia under pressure. In this proof of concept note, we present a hyperbaric chamber for small animals that is used inside an MRI scanner (n=2). It can maintain gaseous anesthesia in the animal throughout the pressurization and decompression experiment, and it allows monitoring of breathing, heart rate, and temperature. Additionally, it has a heat exchanger to warm the breathing gas mixture just before entering the chamber to maintain the animal's body temperature. We present MRI data taken with this setup that show the formation of gas bubbles in the spinal cord of one of two rats in real-time on decompression from 7.1 bar absolute to normobaric conditions.

4.2 Methods

All experiments were conducted under the ethics approval of the Institutional Animal Care and Use Committee (IACUC) at the University of Michigan.

4.2.1 MRI and Pressure Protocol

Images were acquired in a 7 T pre-clinical scanner (Varian, now Agilent), using a 60mm saddle coil manufactured by Morris Instruments. Four- to 6-week-old female Sprague Dawley rats were imaged inside a custom-built MRI-compatible pressure chamber. A standard gradient echomulti-slice (GEMS) sequence was used (TR/TE= 500 ms /2.5 ms, flip angle=30,

voxel size 125 µm × 125 µm × 1000 µm). For this exploratory work we chose a gradient echo sequence because the images are sensitive to both spin density—the absence of spins inside a newly formed bubble—and the field distortions caused by the susceptibility contrast between the empty bubble and the tissue surrounding it. Successive image acquisitions produce a "movie" of the spinal cord with 1 min temporal resolution from frame to frame. To improve the SNR, the images acquired during compression were temporally averaged over four scans for a temporal resolution of approximately 4 min. Similarly, images acquired during decompression were temporally averaged over two scans, for a temporal resolution of approximately 2 min.

With the rat inside the pressure chamber, and the chamber placed in the scanner, the chamber was pressurized to 7.1 bar absolute in 45 s, or $\sim$270 fsw min^{-1}. The pressure was maintained for 45 min, and then decompressed to 1 bar absolute within 30 s, or $\sim$410 fsw min^{-1}. This protocol is known to preferentially induce neurologic DCS in rats and causes little pulmonary barotrauma because of their relatively high ventilatory rates [93]. We show several MRI scans taken from 8 min into the compression phase, to 10 min after decompression.

4.2.2 Image Pre-Processing

The MRI images were processed using OpenCV (v. 4.8), NumPy (v. 1.26), and SciPy (1.12) algorithms programmed in Python [94, 95, 96]. To enhance image quality, each image underwent a two-fold, cubic interpolation, upsampling [96] in both dimensions. Images were registered using a phase correlation algorithm [94] that detects translational shifts in k-space. This alignment was focused on the area containing the spinal cord and vertebrae. A multi-nonlocal means denoising algorithm [94, 97] was then applied using the two temporally closest scans for all images. Further noise reduction and feature edge enhancement were achieved through the implementation of a five-pixel diameter bilateral filter [94]. Last, image contrast was improved using a contrast-limited adaptive histogram equalization algorithm8 on each

image.

4.2.3 Image Segmentation

Following image denoising, the regions of presumptive bubble formation were determined by subtracting the average of the four initial scans from the average of the four final scans, resulting in a difference image. The distribution of the grayscale pixel intensities in the difference image was fitted with a Gaussian. Only pixels where the intensity has changed by more than two SDs were retained. Pixels outside of the spinal cord were further discarded. Contiguous pixels in this segmented image were considered as unique regions of presumptive bubble formation. An additional control region, approximately the size of the other regions, was randomly chosen at the center of the spinal cord. Our image processing script is openly available [98].

4.2.4 Chamber and pressurization system

The cylindrical pressure chamber is machined from solid, transparent polycarbonate. The tube has a total length of 330 mm, an outer diameter of 5.74 mm, and a wall thickness of 3.3 mm. An internal polycarbonate tray supports the rat laid in a supine position. The pressure chamber tube has threads and O-ring seals on both ends to attach an end cap with electric and gas feedthroughs on one end, and a heat exchanger for the inflowing gas on the other end. The electrical feedthroughs connect to the ECG and temperature sensors. A 5/32" OD push-to-connect fitting connects to a pressure sensor (Dwyer Instruments 626-04-GH-P8-E2-S5) to instantaneously monitor the chamber pressure. A second fitting serves as the exit port for the anesthetic gas flow. (Figure 4.1).

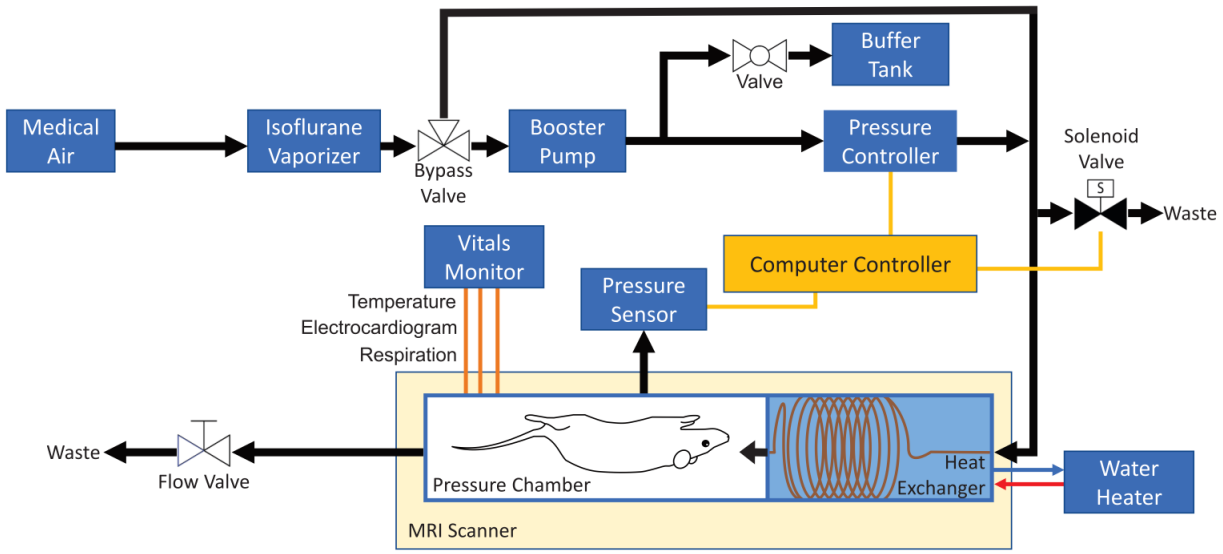

Figure 4.1: Schematic of the chamber and pressurization system. The air pathway is indicated by black arrows, electronic connections are indicated by yellow lines, vital monitoring wiring is indicated by orange lines, and hot water is indicated by a red arrow, whereas cold water is indicated by a blue arrow.

Pressure inside the pressure chamber is controlled with an electronic pressure control system. Medical-grade air, mixed with isoflurane, is compressed by a booster pump (Haskel AGD-4) to 9.3 bar absolute and stored at that pressure in a small buffer tank (Figure 4.1). An electronic pressure-control valve (ProportionAir QPV1MANEEZP100PSGBXN) is used in conjunction with the chamber pressure sensor and custom LABVIEW software to implement the desired pressure profiles in the chamber. An additional solenoid valve (Atlantic Valves BZW-20) is used to quickly depressurize the system, as depressurization through the control valve itself is too slow for our protocol.

4.2.5 Anesthesia and vital monitoring

Because the anesthetic effect of isoflurane depends primarily on the partial pressure rather than its absolute concentration [99], we administered an isoflurane concentration of 0.25% (v/v) to achieve stable anesthesia at 7.1 bar absolute. To simplify anesthetic maintenance at atmospheric pressure before compression and after decompression, we used a bypass valve

to circumvent the booster pump and pressure control equipment during these phases of the experiment. This allowed us to directly feed the output of the evaporator into the pressure chamber at 1% (v/v) isoflurane concentration.

The pressure cell was designed to accommodate commercial MRI-compatible vital monitoring hardware from Small Animal Instruments. This monitoring suite includes the Model 1030 Monitoring and Gating Systems, 3-lead surface ECG electrodes, and a rectal thermistor to monitor the animal's temperature. Respiration is monitored using a technique termed E-RESP by Small Animal Instruments, Inc: the ECG wires are placed to make a loop around the animal's chest (Figure 4.2). As the loop size changes with respiratory motion, a small voltage is induced in the ECG wires, because of the changing magnetic flux through the loop. We used this E-RESP method of respiration monitoring because conventional pneumatic pillows are unsuitable for operation at elevated pressures. Vitals were measured and recorded using the software provided by Small Animal Instruments.

Figure 4.2: A rat is secured on the pressure chamber tray with electrocardiography wires arranged in an E-RESP configuration, which consists of a wire looped around its chest to generate induced voltage changes from respiratory movements in the presence of a magnetic field, and an inserted rectal temperature sensor.

To compensate for heat loss in the animal during imaging, it is not sufficient to warm it by blowing heated air through the bore of the MRI scanner because the RF coil and the pressure chamber occupy most of the MRI bore in our set-up. Therefore, the breathing air is warmed as it enters the chamber with an MRI-compatible heat exchanger that is mounted at the gas inlet end of the pressure chamber. The heat exchanger consists of a small compartment through which warm water is circulated. The breathing gas flows through a 5 m copper tubing coil that is in direct contact with the warm water. The temperature of the warm water can be manually adjusted to maintain the appropriate body temperature of the animal and is typically set to 40 °C to raise the pressure chamber temperature by ∼3 °C.

4.3 Results

We successfully compressed two live rats inside the MRI scanner to 7.1 bar absolute for 25 min before decompressing them and maintaining them anesthetized at atmospheric pressure until they succumbed to severe DCS. Real-time MRI scans during this process showed the formation of decompression bubbles in the spinal cord in both rats, but only one is shown here. Figure 4.3A, left, shows an axial image slice of the thoracic region in the compressed rat, before bubble formation. Figure 4.3A, right, taken ∼10 min after decompression and around the time of the rat's expiration, displays a large gas bubble (1) in the posterior median spinal vein. A smaller gas bubble (2) in the nervous tissue of the spinal cord is also visible. We further note bubble-like entities (3–5) near the anterior region, which may indicate bubble formation between the pia mater and white matter. The right lateral region of the spinal cord (6) is also significantly distorted, but we cannot conclusively associate them with anatomical features of the rat.

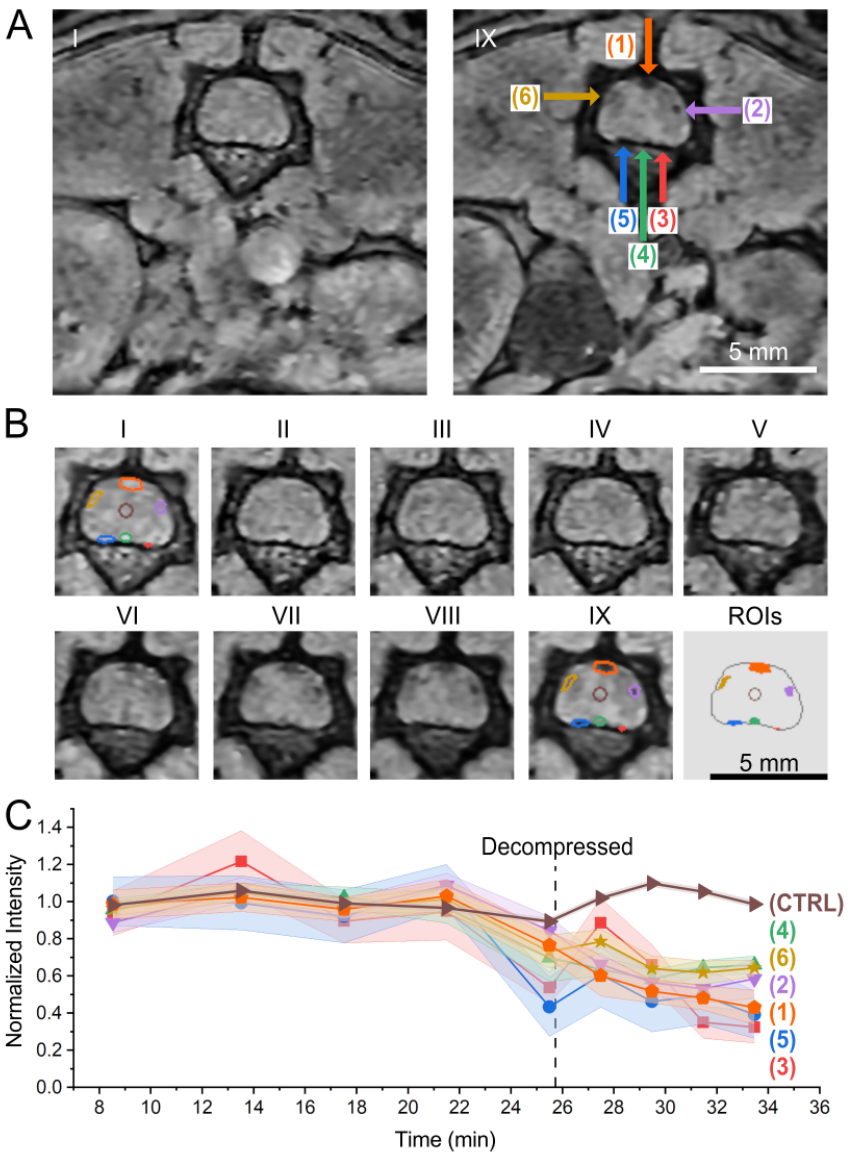

Figure 4.3: MR images of the spinal region of a rat (A) (left) after pressurization to 7.1 bar absolute and (right) 10 minutes after decompression to 1 bar absolute. The second image shows a gas bubble in the posterior median spinal vein (1), one other suspected gas bubble (2), and several distorted spinal cord regions (3-6). The right third of the spinal cord is darker near (2), possibly indicating hemorrhage. (B) A time series of MRI scans of the spinal cord taken during the experiment are shown. The last panel shows the regions of interest (ROIs) as discussed in Methods, as well as an additional control region (CTRL) located in the center of the ROIs panel. Each region of interest was used to determine the (C) average intensity over the series of images to determine the appearance of bubble formation. The intensity timepoints indicate the start of the MRI scan. The bubble in the posterior median spinal vein is shown in orange (1), the other suspected bubble is shown in purple (2), a non-bubble control region is shown in brown (CTRL), and other significant spinal cord distortions are shown (3-6).

The evolution of bubble formation is shown in Figure 4.3B. The images, while the chamber was compressed (I–IV), showed no significant change, whereas images post decompression (VI–IX), revealed bubbles. Images VI–VIII showed potential left and right lateral vein fracturing occurring that may be responsible for the appearance of hemorrhaging near the second smaller bubble (2). Several regions of interest are shown in Figure 4.3B-I,4.3B-IX to determine the change in average intensity, including a control region. As indicated in Figure 4.3C, the average intensity decreases with the formation of a bubble in the posterior median spinal vein (1), in the left lateral most bubble (2), and along the distorted anterior and right lateral regions of the spinal cord (3–6), but not in the non-bubble control region (CTRL).

Continuous monitoring of respiration rate, heart rate, and temperature was conducted during pressure changes, as depicted in Figure 4.4. Adequate anesthetic depth was successfully maintained throughout the experiment as confirmed via stable vitals. The heart rate stayed around 300 beats per min and the respiratory rate was ∼30 to 35 breaths per min until the rat expired.

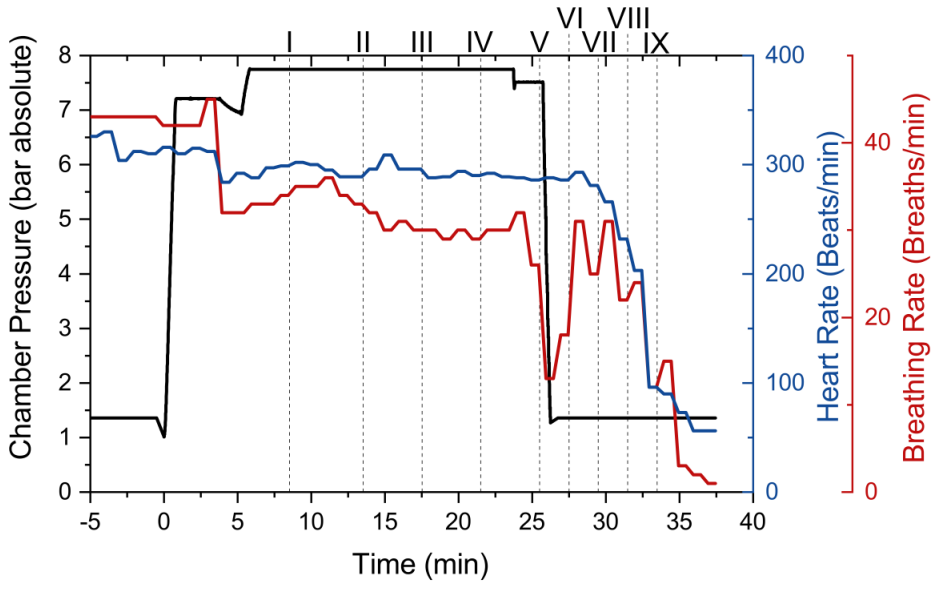

Figure 4.4: Heart rate and respiratory rate of the rat during compression and decompression. The vertical dashed lines indicate the times at which MRI scans were taken and correspond to those shown in Figure 4.3.

4.4 Discussion and Conclusions

Decompression sickness symptoms are closely related to the formation of inert gas bubbles in the body [90]. The exact pathophysiology of how gas bubbles in deeper tissues form, and subsequently dissolve on treatment through recompression remains largely mysterious, as gas bubbles in the spinal cord and similar tissues could only be observed through histopathology until now. Our novel combined pressurization and imaging method allows the observation of decompression gas bubble formation in a live animal under anesthesia in a pressure chamber inside the MRI scanner in real time. We demonstrate a 125 µm voxel resolution for a stack of 30 3.25 cm $\times$ 1.6 cm images. This resolution is achieved with four averages for a 4-min scan pre-decompression and two averages for a 2-min scan post-decompression.

We observed the formation of a large bubble with a cross section of $\sim$0.4 mm^2 in the largest vein of the spine, the posterior median spinal vein, and a smaller bubble in another area of the spinal cord. The physical deformations and distortions of the tissue surrounding the bubbles in response to their rapid growth may have led to direct mechanical damage of the tissue and local hemorrhage, eventually leading to the demise of the animal.

In conclusion, we have shown that it is possible to observe the growth of decompression gas bubbles in real time in live rats using MRI in conjunction with a purpose-built pressure cell and life support and monitoring equipment. Using an aggressive compression and decompression protocol that is known to preferentially induce SC-DCS, we were able to observe the formation of gas bubbles in the spinal cord until the animal expired from the damage. Maintenance and monitoring of anesthesia were possible at isoflurane concentrations that are largely determined by the partial pressure of the anesthetic during the various stages of the experiment. This new capability will enable rigorous testing of many of the assumptions that are made in understanding the pathophysiology of deep-tissue DCS and its treatment though recompression without having to rely solely on histopathology.

4.5 Future Direction

The pressure chamber discussed here is a proof of concept for visualizing in vivo spinal cord decompression bubbles. This work can be improved by incorporating a surface coil near the spinal cord and performing a thorough optimization of imaging parameters to modestly improve resolution. Regardless of these proposed improvements, we can now examine the effects of oxygen and other gas mixtures after during changes in pressure and the effects of varying ambient pressure on spinal cord decompression bubbles.

CHAPTER 5

Conclusions

In conclusion, our research provides significant insights into the complex nature of spinal cord decompression sickness (SC-DCS) by demonstrating the mechanical damage caused by decompression gas bubbles and the limitations of the current elastic bubble theory. In Chapter 2, we presented evidence of direct mechanical damage to ex vivo bovine spinal cord tissue caused by growing decompression gas bubbles, which cannot be adequately explained by a reversible elastic response of the surrounding tissue. Our findings suggest that the forces involved in gas bubble growth are sufficient to exceed the yield stress of the tissue, resulting in tearing or viscoelastic deformation of the nerve tissue. These findings highlight the importance of considering SC-DCS as a multifaceted condition that may require a comprehensive approach in its treatment, going beyond shrinking the offending gas bubble and reoxygenating tissue to address the traumatic nature of the injury.

In Chapter 3, we extended the analysis of the coupled tissue-gas mechanics model from Chapter 2 to gain a deeper understanding of the role of tissue and gas mechanics at different timescales, under different decompression profiles, and with varying bubble sizes. Our analysis suggests that tissue mechanics plays a significant role in the resulting average surface stress of bubbles and that recompression can result in a similar stress profile as decompression. These findings are counter to the well assumed elastic bubble theory and suggest that recompression can do as much damage as decompression. We also identified limitations in our model, observed at the micrometer scale, but we nonetheless identified that diffusion

effects dominate decreasing bubble sizes while tissue mechanics dominate larger bubbles. The combined effect of these mechanics leads to a plethora of possible dynamic behavior in decompression bubbles and tissue.

In Chapter 4, we developed a novel pressure chamber system compatible with rodent vital monitoring and MRI to monitor the growth and development of decompression gas bubbles in real-time. We demonstrated the presence of decompression gas bubbles in the spinal cord after compression to 7.1 bar absolute and rapid decompression while maintaining a stable anesthetic depth. We observed decompression gas bubbles in various locations, including the posterior median spinal vein, near the spinal meninges, and other regions. We also observed possible signs of hemorrhage surrounding near the left most lateral bubble. With this system, we can test many of the aforementioned empirical recommendations for managing SC-DCS and quantify their effect on the spinal cord.

Moving forward, it is essential to understand and implement other tissue and gas mechanics, such as physiological relevant tissue parameters at long timescales, spinal cord behavior with accurate damage models, micrometer strain gradients, and competing micrometer diffusion time scales to fully model the mechanics of decompression bubbles at all scales. For visualizing in vivo bubbles, it may be necessary to modify the system to assess other conditions, such as the effect of multiple breathing gases and testing hypobaric conditions - mimicking aerospace conditions. A thorough imaging optimization may also lead to a necessary improvement in bubble resolution.

Our research provides a solid foundation for the development of new, safe decompression models for aeronautical and diving activities based on physiologically relevant biophysical principles. The combination of our experimental and theoretical tools can pave the way for a more comprehensive understanding of SC-DCS and its management.

APPENDIX A

Complete Circuit Diagrams for In Vivo Pressure Chamber Manifold

This appendix provides detailed circuit schematics used to control the pressure throughout the pressure chamber manifold system.

A.1 Circuit 1 – Manifold Power Distribution

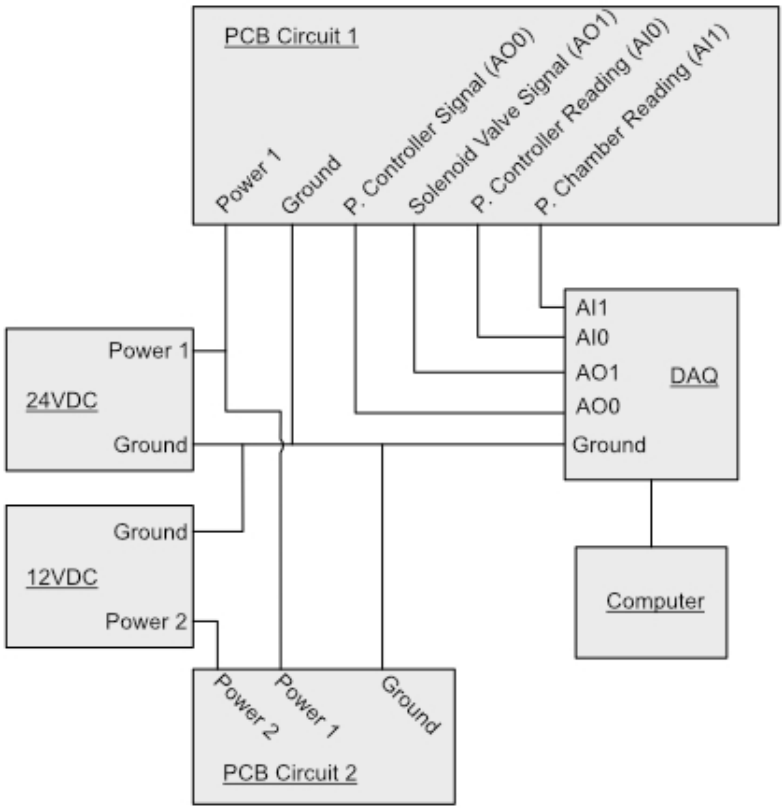

Figure A.1: The electronic schematic is shown for power distribution across the pressure chamber manifold. One analog output is used to control the pressure controller (AO0) and the other is used to control the decompression solenoid valve in PCB Circuit 1 (AO1). The pressure controller also has an analog input to monitor the local pressure (AI0). A second analog input is used to monitor the pressure from the pressure chamber (AI1). PCB Circuit 2 controls the output pressure of the gas booster in the intermediate buffer tank.

A.2 PCB Circuit 1 – Decompression Control Rate

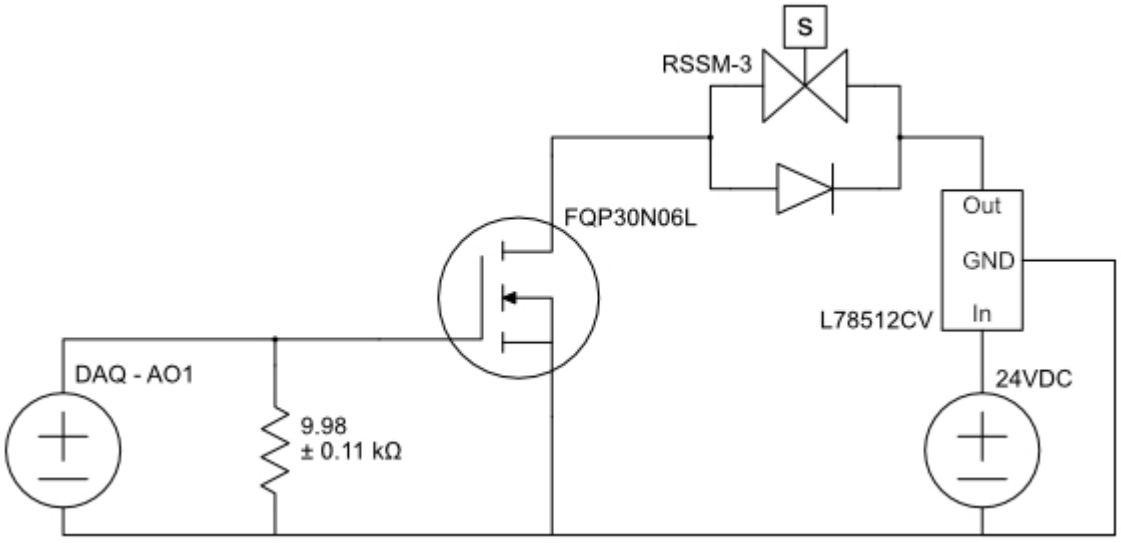

Figure A.2: The circuit shown controls the rate of decompression. If the rate of decompression is not fast enough, the DAQ outputs a signal to control the opening of an additional, normally closed, solenoid valve outlet to increase the rate of decompression. The solenoid valve may open several times during decompression.

A.3 PCB Circuit 2 – Pressure Control in Tank Buffer

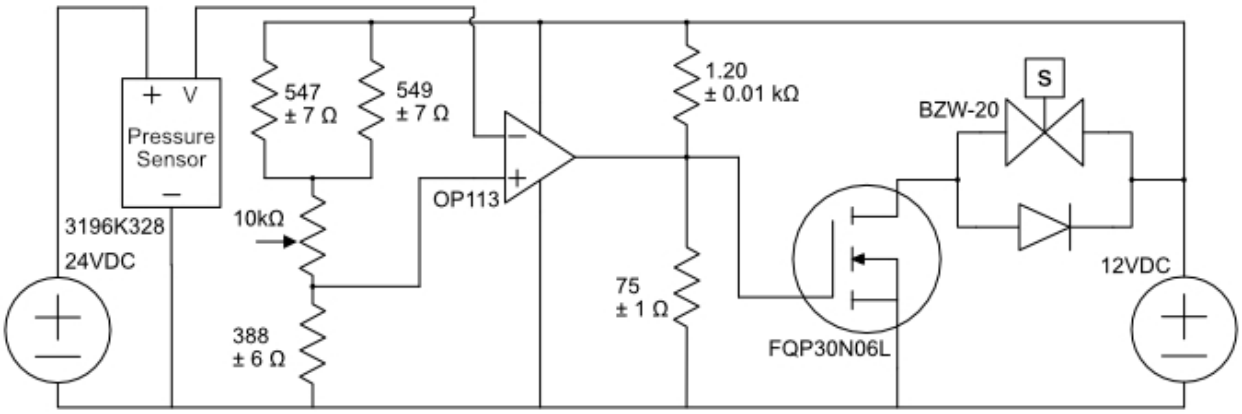

Figure A.3: The pressure in the buffer tank is controlled with the analog circuit shown. The pressure is measured and controls the opening and closing of the normally closed solenoid valve that regulates air intake into the gas booster. The upper pressure limit is controlled by the potentiometer with a maximum tank pressure of 135 psi. This limit is imposed to prevent mechanical failure of the bronze tubing.

APPENDIX B

In Vivo Pressure Chamber Manifold Operation Protocol

This appendix provides the protocol to operate the in vivo pressure chamber manifold in conjunction with the LABVIEW file described in Appendix C. The following appendix lists one typical compression/decompression cycle experiment in the MRI room. It may be necessary to modify the system or workflow for operating this system outside of the MRI room depending on equipment availability. This system can perform various consecutive pressure cycles by repeating Stage 5 and 6 as necessary. Finally, it is best to memorize Stages 5 and 6 to ensure the rat is always receiving a steady supply of isoflurane mix.

Stage 1: Manifold Setup

1. Close air compressor exhaust ports and connections.
2. Turn on the air compressor to fill to max.
3. Meanwhile, check all electrical connections in the In Vivo Pressure Chamber Manifold.
4. In LabView, press "depressurize" button to ensure system is electrically zeroed. The system will audibly beep when pressure is zero.
5. Close intermediate tank output (V1 - green label).

6. Open the intermediate tank valve (V2 – blue label)

7. Change the three-way valve airflow to include the gas booster (MV1 - left-down).

8. Open regulator for the gas cylinder of choice to 10 psi.

9. Provide the vaporizer with 5psi using the precision regulator. You will hear a buzz and a soft click from the gas booster.

10. Set the vaporizer concentration. Since the efficacy of anesthesia decreases at higher pressures, it's best to slightly overestimate the amount of isoflurane needed. At minimum, the desired output concentration is set according to the equation:

$$c_e = \frac{c_d}{P_d} \tag{B.1}$$

where c_e is the equivalent dial concentration, c_d is the desired concentration at 1 ATA, and P_d is the target pressure in ATA.

11. Set air compressor output to 50 psi.

12. Flip solenoid switch (SW1) to fill the intermediate tank.

13. Wait for gas booster to automatically shut off, indicative of max pressure reached, and close intermediate tank valve (V2 - blue label).

14. Turn the solenoid switch off (SW1).

15. Turn the air compressor off to reduce water intake in the air compressor.

16. Close the gas cylinder tank supply to the vaporizer.

17. To easier screw the chamber together at a later time, it is best to wrap the output tubing of the pressure chamber around the pressure chamber itself after it's been connected. This tubing is wrapped with white electrical tape. Wrap the tubing 10x in the direction of the arrow indicated on the pressure chamber and secure with tape.

18. Uncoil any twists in the remaining output tubing and the tubing connected to the chamber sleeve end.

19. Place the wrapped pressure chamber into the RF coil.

20. Place the output of the manifold flow meter into the gas collection system.

Stage 2: Rat Preparation

1. Ensure direction of airflow to induction chamber from oxygen gas cylinder and leads to the gas collection system.

2. Ensure the heat pad under the induction chamber and the heat pad to the right of the induction chamber is on.

3. Insert absorbent paper towels into the induction chamber.

4. Use 4-5% isoflurane to fill induction chamber at a rate of 1L/min.

5. Prior to handling rat, ensure the face mask output has minimal suction pressure by testing this on your skin. Reduce the gas collection system flow rate as needed. This ensures the isoflurane mix reaches the rat and is not preemptively removed.

6. Place rat into induction chamber and wait until movement has ceased and breathing has steadied at about 70-110 breaths/min. Test the level of anesthetic depth by squeezing their paw relatively hard. The rat should not react.

7. Change isoflurane to 2% at 1L/min and flow through the face mask.

8. Place rat on inner chamber sleeve, stomach up, and attach the face mask. The chamber sleeve should be placed on the heat pad out to the right of the induction chamber.

9. Apply ophthalmic ointment to eyes to prevent them from drying.

10. Lubricate and insert rectal thermometer – secure with surgical tape to base of tail

11. Fill ECG electrodes with conduction gel and secure to paws with surgical tape. Red/black wires should be secured to the front paws. The third wire can be attached to any back paw.

12. One of the wires secured to the front paw should be secured, with painter's tape, across the chest of the rat for E-RESP.

13. Attempt to twist wires together near the base of the rat. Any additional loose wires should be secured to the rat and/or chamber sleeve with surgical tape.

Stage 3: Rat Maintenance in Pressure Chamber

1. On the pressure chamber manifold, change the three-way valve airflow to include the gas chamber (MV1 - left-up).

2. Open the gas cylinder tank regulator to the vaporizer and set the output pressure to 10 psi.

3. Ensure 2% isoflurane mix is flowing through the pressure chamber either by wafting the output towards you or by testing for pressure when temporarily covering the output with your hand.

4. Screw the pressure chamber together with the rat inside, ensuring the rat remains in the same orientation. When closed, the pressure chamber should be tight when chamber cap markings align. Do not over tighten or there is a risk of displacing the inner O-ring.

5. Ensure the rat is receiving 1 L/min on the manifold flow meter.

Stage 4: Rat Preparation in the MRI machine

1. Connect the temperature probe and ECG wire outputs to the ERT Module. The black and red ERT Module inputs correspond to the front paw connections. See the ERT Manual for setting up E-Resp.

2. Ensure the rat temperature is between 35.9°C and 37.5°C. This can be done with the water heater system or with the in-house air heater system at higher temperatures.

3. Calibrate image acquisition as necessary on the MRI machine.

4. When ready to pressurize, turn on the air compressor.

5. In LabVIEW, load parameters or customize pressure profile as needed. See Appendix 3 for more information.

Stage 5: Pressurize System

Perform quickly to maintain 1L/min. Reverse steps during decompression.

1. Open the intermediate tank valve (V2 - blue label).

2. Change vaporizer output to desired concentration. This should match the concentration used to fill the intermediate tank.

3. Change three-way valve flow through pressure chamber (MV1 - left-down).

4. Turn on solenoid valve (SW1).

5. In LabVIEW, press Pressurize.

6. Maintaining flow rate at 1L/min while pressure builds.

Stage 6: Depressurize System

The system will automatically depressurize according to the pressure profile.

1. Maintaining flow rate at 1L/min while pressure depletes.

2. The system will audibly beep three times when the pressure is near 0 psi. Perform the following after this beep.

3. Turn off solenoid valve (SW1).

4. Change vaporizer output to 2%.

5. Change three-way valve flow through gas booster chamber (MV1 - left-up).

6. Close the intermediate tank valve (V2 - blue label).

Stage 7: Cleanup

1. Between different rats, ensure the system is clean with ULAM approved wipes. At the end of the day, rinse pressure chamber that houses rat with soap and water.

2. Empty the intermediate buffer tank.

3. Ensure the isoflurane vaporizer concentration dial is set to zero.

4. Pack the remaining system away as necessary.

APPENDIX C

LabVIEW Virtual Instrument (VI) for In Vivo Pressure Chamber Manifold

This appendix provides an outline of the LabVIEW VI v.2023 used to control the pressure of the in vivo pressure chamber manifold system. Use in conjunction with Appendix B.

C.1 Front Panel

The front panel is a one-page user interface, as shown in Figure C.1, that takes user specified values to generate a voltage waveform to control an electronic pressure controller (ProportionAir QPV1MANEEZP100PSGBXN). A second pressure sensor (Dwyer Instruments 626-04-GH-P8-E2-S5) monitors the pressure in the pressure chamber.

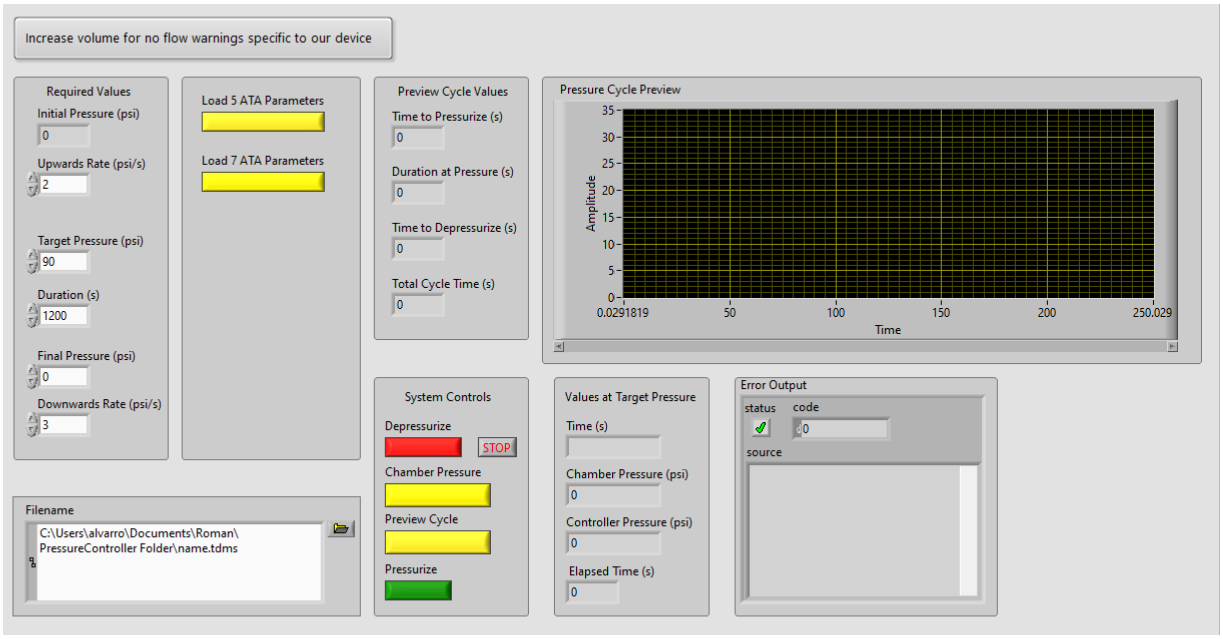

Figure C.1: The Front Panel of the LabVIEW VI for the In Vivo Pressure Chamber Manifold.

C.1.1 Numeric User Inputs

To pressurize the system, the user must provide the following parameters:

Input Text	**Description and Additional Notes**
Upwards Rate (psi/s)	The rate at which the system should pressurize. Two psi/s is the fastest rate to pressurize to 90 psi accurately.
Target Pressure (psi)	The pressure the system should maintain.
Duration (s)	The time the system should maintain the target pressure.
Downwards Rate (psi/s)	The rate at which the system should depressurize. Aim to decompress the system in 30s.
Final Pressure (psi)	The pressure the system should depressurize to.

Table C.1: Required numeric inputs to pressurize chamber.

It is also recommended, but not necessary, to specify a file path where system time, pressure of chamber, and pressure from the controller are recorded to. The filename should end with *.tdms for LabVIEW to write to it correctly.

C.1.2 Numeric User Inputs

There are several buttons associated with the system. Each functionality is described in Table C.2.

C.2 Back Panel

The block diagram is what controls the pressure in the pressure chamber after the user specifies the required inputs discussed in Table C.1 and seen in the left column of Fig. C.2. The block diagram consists of four main groups. The left panel indicates the required user inputs, the center conditional loop depends on the button pushed, the top right reports the 'Preview Cycle Values,' and the bottom right controls the continuous while loop with a slight delay to detect user input.

We will only discuss the main conditional loop, which is in effect when the Pressurize button is selected. It consists of three main loops and a SubVI. The first timed loop, center right, pressurizes the system at the 'Upwards Rate' specified. The second while loop, center bottom-left, maintains the pressure in the chamber to within 1 psi of the specified target pressure. There is additional logic that operates similar to a PID controller. The last timed loop, center bottom-right, depressurizes the system. There is additional logic to open the exhaust solenoid if the pressure is not following the ideal specified 'Downwards Rate.' The main loops are encased in a Boolean condition to generate waveforms dependent on the required input parameters. For instance, the user can specify the final pressure to be the same as the target pressure; skipping over the last loop to prevent system decompression.

C.2.1 SubVI

The SubVI takes the user inputs as specified in Table C.1 to generate a preview of the target waveform. A DAQ Assistant is setup to read 500 samples and average them to update the chamber pressure.

Button Name	**Description and Additional Notes**
Load 5 ATA Parameters	This button will prefill the required parameters for a typical 5 ATA experiment. The parameters are as follows: Upwards Rate = 3, Target Pressure = 60, Duration = 3600, Downwards Rate = 3, Final Pressure = 0.
Load 7 ATA Parameters	This button will prefill the required parameters for a typical 7 ATA experiment. The parameters are as follows: Upwards Rate = 3, Target Pressure = 90, Duration = 1800, Downwards Rate = 3, Final Pressure = 0.
Chamber Pressure	This button will manually update the current pressure in the chamber. It is useful to monitor what the system pressure is set to.
Preview Cycle	Upon entering the required parameters in Table C.1, the user can visualize the generated waveform from these parameters in the plot window titled "Pressure Cycle Preview." In addition to inspecting the generated plot, the 'Preview Cycle Values' will also populate with the expected time duration to complete each experimental section.
Depressurize	This button is only to be used for emergency purposes. Unfortunately, the system cannot be interrupted without stopping the VI. Therefore, the user must 'STOP' the VI first, Start the VI, and then select Depressurize.
Pressurize	This button will proceed to pressurize the system according to the specified entered parameters listed in Table C.1. It is recommended to first preview the cycle to ensure the system behaves as expected. Once the system reaches the target pressure, the 'Values at Target Pressure' will populate with the current pressure and elapsed time at pressure. Once this value reaches the specified 'Duration (s)' value, the system will automatically depressurize.

Table C.2: A list of buttons and their descriptions to control the pressure chamber.

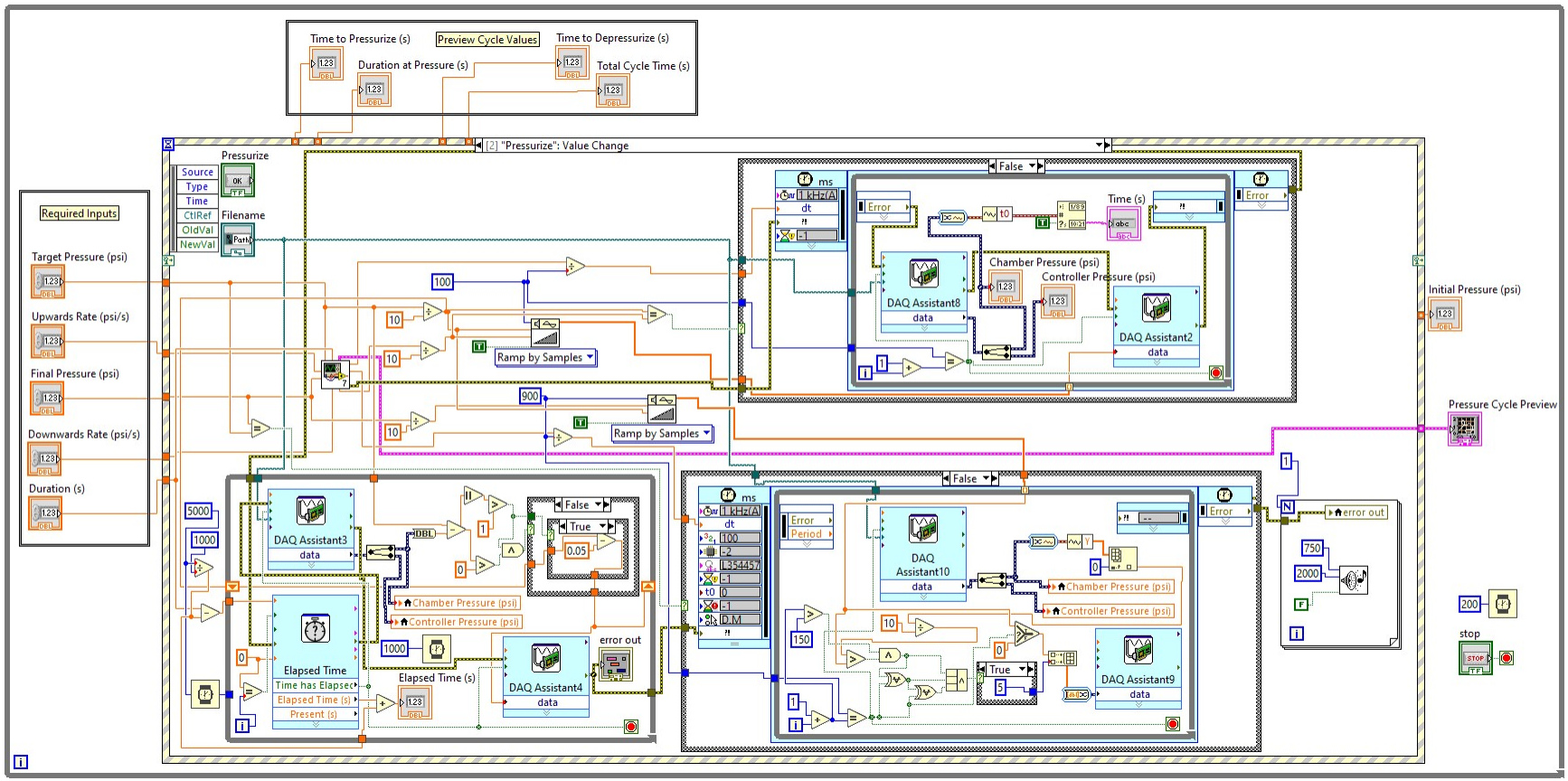

Figure C.2: The block diagram to control the pressure in the pressure chamber is shown. The three main loops, in order of operation, are pressurization (top right), pressure maintenance (bottom left), and depressurization (bottom right).

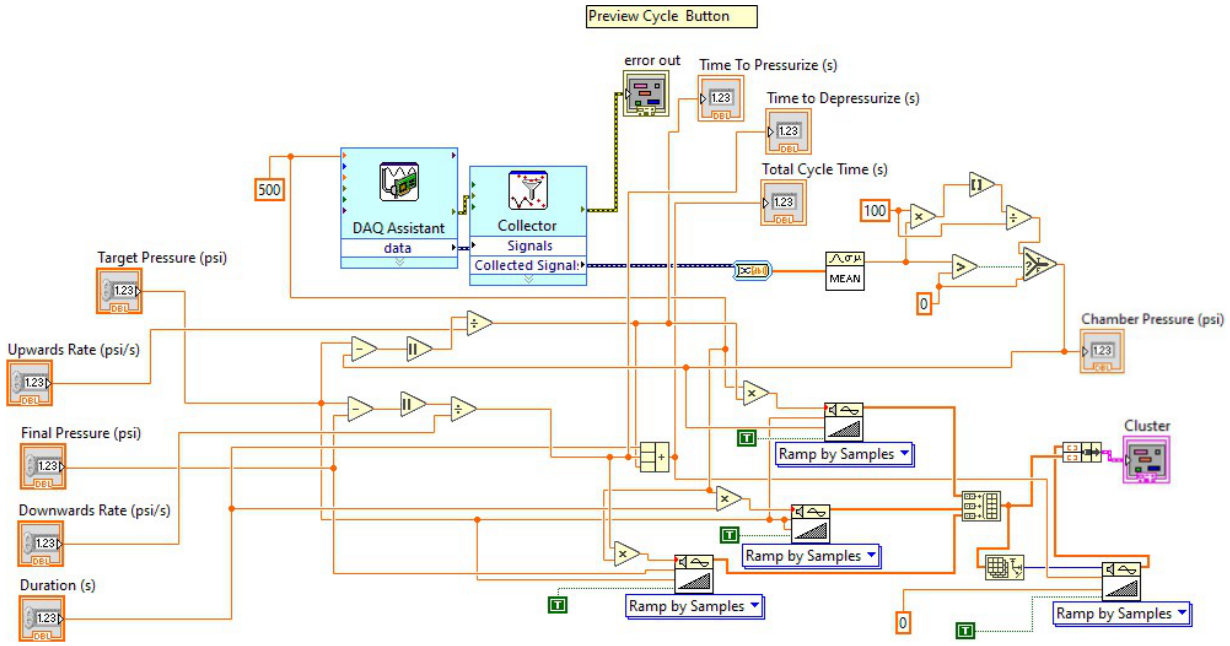

Figure C.3: The SubVI shown in C.1, used to generate a waveform an update the current chamber pressure.

C.2.2 DAQ Configuration

Each DAQ Assistant Express VI is setup to acquire data one sample on demand. This ensures the DAQ is operating at precision times as specified by the timed loops. Additionally, the DAQ was configured to have two channels. The scaling equations for the pressure measured in the chamber is

$$p_c = \left(19.5\frac{psi}{V}\right) V_d - 13.7psi \tag{C.1}$$

and the scaling for the pressure measured by the controller is

$$p_r = \left(10.0\frac{psi}{V}\right) V_d \tag{C.2}$$

where V_d is the voltage measured by each device.

C.3 Future Enhancements

One potential drawback of this system is the logic implemented in the second main loop to maintain pressure. It is currently designed to maintain pressure even if the system has a leak. Therefore, the system will continuously send a signal to constantly increase the output pressure. If the system is fixed while the system is running, this will cause the system to pressurize above the target pressure. The max output pressure is 100 psi, well below equipment failure point, but it is best practice to either (1) fix this with an implemented "leak detecting logic" in the loop, or (2) abort fixing the system if there is any equipment failure.

BIBLIOGRAPHY

[1] K. Ichihara, T. Taguchi, Y. Shimada, I. Sakuramoto, S. Kawano, and S. Kawai. Gray Matter of the Bovine Cervical Spinal Cord is Mechanically More Rigid and Fragile than the White Matter. *J. Neurotrauma*, 18(3):361—367, 2001.

[2] J.R. Rubmble. *CRC Handbook of Chemistry and Physics, 104th Edition*. CRC Handbook of Chemistry and Physics, 104th Edition, 2023.

[3] S. Ninokawa and K. Nordham. Discovery of caisson disease: a dive into the history of decompression sickness. *Proc (Bayl Univ Med Cent)*, 35(1):129–132, 2022.

[4] A.A. Bove and J.C. Davis. *Diving Medicine, 4th ed*. Saunders, 2003.

[5] W.P. Butler. Caisson disease during the construction of the Eads and Brooklyn Bridges: A review. *Undersea Hyperb Med*, 31(4):445–59, 2004.

[6] P.K. Weathersby and L.D. Homer. Solubility of inert gases in biological fluids and tissues: a review. *Undersea Biomed Res*, 7(4):277–96, 1980.

[7] C.A. Ward, P. Tikuisis, and R.D. Venter. Stability of bubbles in a closed volume of liquid-gas solution. *J Appl Phys*, 53(9):6076–6084, 1982.

[8] S. Goldman. Generalizations of the Young–Laplace equation for the pressure of a mechanically stable gas bubble in a soft elastic material. *J Chem Phys*, 131(18):184502, 2009.

[9] A. Brubakk and T. Neuman. *Bennett and Elliott's Physiology and Medicine of Diving*. Saunders Limited, 2003.

[10] V.P. Katuntsev. Decompression sickness-one of the vital problems of aerospace medicine. *Aviakosm Ekolog Med*, 32(6):11–20, 1998.

[11] J.M. Hallenbeck. Cinephotomicrography of dog spinal vessels during cord-damaging decompression sickness. *Neurology*, 26(2):190–190, 1976.

[12] F.M. Jardine and R.I. McCallum. *Engineering and Health in Compressed Air Work*. E&FN Spon, 1994.

[13] C. Chryssanthou, J. Kalberer, S. Kooperstein, and W. Antopol. Studies on Dysbarim II. Influence of Bradykinin and Bradykinin-Antagonists on Decompression Sickness in Mice". *Aerosp Med*, 35:741–746, 1964.

[14] T.B. Buttolph, E.J. Dick, C.B. Toner, J.R. Broome, R. Williams, Y.H. Kang, and N.L. Wilt. Cutaneous lesions in swine after decompression: histopathology and ultrastructure. *Undersea Hyperb Med*, 25(2):115–21, 1998.

[15] A.R. Behnke. A review of physiological and clinical data pertaining to decompression sickness. Technical Report 4, Naval Medical Research Institute, 1945.

[16] A.C. Palmer, W.F. Blakemore, and A.G. Greenwood. Neuropathology of Experimental Decompression Sickness (Dysbarism) in the Goat. *Neuropathol Appl Neurobiol*, 2(2):145–156, 1976.

[17] A.P.K. Dick and E.W. Massey. Neurologic presentation of decompression sickness and air embolism in sport divers. *Neurology*, 35(5):667–667, 1985.

[18] S.J. Mitchell and D.J. Doolette and C.J. Wacholz and R.D. Vann. Management of mild or marginal decompression illness in remote locations: workshop proceedings. Technical report, Divers Alert Network, 2005.

[19] F.C. Golding, P. Griffiths, H.V. Hempleman, W.D.M. Paton, and D.N. Walder. Decompression Sickness during Construction of the Dartford Tunnel. *Br J Ind Med*, 17(3):167, 1960.

[20] T.J. Francis, J.L. Griffin, L.D. Homer, G.H. Pezeshkpour, A.J. Dutka, and E.T. Flynn. Bubble-induced dysfunction in acute spinal cord decompression sickness. *J Appl Physiol*, 68(4):1368–1375, 1990.

[21] S.J. Mitchell. Decompression illness: a comprehensive overview. *Diving Hyperb Med Journal*, 54(1(Suppl)):1–53, 2024.

[22] I.T. Demchenko, A.E. Boso, M.J. Natoli, P.O. Doar, T.J. O'Neill, P.B. Bennett, and C.A. Piantadosi. Measurement of cerebral blood flow in rats and mice by hydrogen clearance during hyperbaric oxygen exposure. *Undersea Hyperb Med*, 25(3):147–52, 1998.

[23] J.M. Hallenbeck, A.A. Bove, and D.H. Elliott. Mechanisms underlying spinal cord damage in decompression sickness. *Neurology*, 25(4):308–308, 1975.

[24] S.R. Thom, M. Bennett, N.D. Banham, W. Chin, D.F. Blake, A. Rosen, N.W. Pollock, D. Madden, O. Barak, A. Marroni, C. Balestra, P. Germonpre, M. Pieri, D. Cialoni, P.-N.J. Le, C. Logue, D. Lambert, K.R. Hardy, D. Sward, M. Yang, V.B. Bhopale, and Z. Dujic. Association of microparticles and neutrophil activation with decompression sickness. *J Appl Physiol*, (119):427–343, 2015.

[25] C.A. Ward, D. McCullough, D. Yee, D. Stanga, and W.D. Fraser. Complement activation involvement in decompression sickness of rabbits. *Undersea Biomed Res*, 17(1):51–66, 1990.

[26] L.L. Levin, G.J. Stewart, P.R. Lynch, and A.A. Bove. Blood and blood vessel wall changes induced by decompression sickness in dogs. *J Appl Physiol*, 50(5):944–949, 1981.

[27] K. Zhang, D. Wang, Z. Jiang, X. Ning, P. Buzzacott, and W. Xu. Endothelial dysfunction correlates with decompression bubbles in rats. *Sci Rep*, 6(1):33390, 2016.

[28] A.O. Brubakk and A. Møllerløkken. The role of intra-vascular bubbles and the vascular endothelium in decompression sickness. *Diving Hyperb Med*, 39(3):162–9, 2009.

[29] A.C. Palmer. Nature and incidence of bubbles in the spinal cord of decompressed goats. *Undersea Hyperb Med*, 24(3):193–200, 1997.

[30] P. Bert. *Barometric Pressure (La Pression Barométrique)*. Undersea Medical Society, 1978.

[31] T.D. Kunkle and E.L. Beckman. Bubble dissolution physics and the treatment of decompression sickness. *Med Phys*, 10(2):184–190, 1983.

[32] J. Aharon-Peretz, Y. Adir, C.R.Gordon, S. Kol, N. Gal, and Y.Melamed. Spinal Cord Decompression Sickness in Sport Diving. *Arch Neurol*, 50(7):753–756, 1993.

[33] J.-E. Blatteau, E. Gempp, P. Constantin, and P. Louge. Risk factors and clinical outcome in military divers with neurological decompression sickness: influence of time to recompression. *Diving Hyperb Med*, 41(3):129–34, 2011.

[34] A. Boussuges, X. Thirion, P. Blanc, F. Molenat, and J.M. Sainty. Neurologic decompression illness: a gravity score. *Undersea Hyperb Med*, 23(3):151–5, 1996.

[35] I. Grover, W. Reed, and T. Neuman. The SANDHOG criteria and its validation for the diagnosis of DCS arising from bounce diving. *Undersea Hyperb Med*, 34(3):199–210, 2007.

[36] M.P. Spencer. Decompression limits for compressed air determined by ultrasonically detected blood bubbles. *J Appl Physiol*, 40(2):229–235, 1976.

[37] S. Daniels. Ultrasonic monitoring of decompression procedures. *Philos Trans R Soc Lond B Biol Sci*, 304(1118):153–175, 1984.

[38] S.L. Blogg, M. Gennser, A. Møllerløkken, and A.O. Brubakk. Ultrasound detection of vascular decompression bubbles: the influence of new technology and considerations on bubble load. *Diving Hyperb Med*, 44(1):35—44, 2014.

[39] M. Reuter, K. Tetzlaff, A. Hutzelmann, G. Fritsch, J.-C. Steffens, E. Bettinghausen, and M. Heller. MR imaging of the central nervous system in diving-related decompression illness. *Acta Radiol*, 38(6):940–944, 1997.

[40] J. Hierholzer, A. Tempka, C. Stroszczynski, F. Amodio, N. Hosten, J. Haas, and R. Felix. MRI in decompression illness. *Neuroradiology*, 42(5):368–370, 2000.

[41] P.L. Kei, C.T. Choong, T. Young, S.H. Lee, and C.C.T. Lim. Decompression Sickness: MRI of the Spinal Cord. *J Neuroimaging*, 17(4):378–380, 2007.

[42] R.E. Moon and S. Mitchell. Hyperbaric treatment for decompression sickness: current recommendations. *Undersea Hyperb Med*, 46(5):685–693, 2019.

[43] J.K. Tatuene and R. Pignel and P. Pollak and K.O. Lovblad and A. Kleinschmidt and M.I. Vargas. Neuroimaging of Diving-Related Decompression Illness: Current Knowledge and Perspectives. *AJNR Am J Neuroradiol*, 35(11):2039–2044, 2014.

[44] G. Sparacia and A. Banco and B. Sparacia and M. Midiri and G. Brancatelli and M. Accardi and R. Lagalla. Magnetic resonance findings in scuba diving-related spinal cord decompression sickness. *MAGMA*, 5(2):111–115, 1997.

[45] A.E. Boycott, G.C.C. Damant, and J.S. Haldane. The Prevention of Compressed-air Illness. *J Hyg (Lond)*, 8(3):342–443, 1908.

[46] J.A. Hawkins, C.W. Shilling, and R.A. Hansen. A suggested change in calculating decompression tables for diving. *Naval Medical Bulletin*, 33, 1935.

[47] O.V.D. Aue and R.J. Kellar and E.S. Brinton and G. Barron and H.D. Gilliam and R.J. Jones. Surface decompression, derivation and testing of decompression tables with safety limits for certain depths and exposures. Technical report, US Navy Experimental Diving Unit, 1945.

[48] J. Hugon. Decompression models: review, relevance and validation capabilities. *Undersea Hyperb Med*, 41, 2014.

[49] A.A. Bühlmann. *Decompression — Decompression Sickness*. Springer-Verlag Berlin Heidelberg, 1984.

[50] J.A. Dovenbarger and D.M. Uguccioni. Report on Decompression Illness and Diving Fatalities. Technical report, Divers Alert Network, 1997.

[51] E.J. Dick, J.R. Broome, and I.J. Hayward. Acute neurologic decompression illness in pigs: lesions of the spinal cord and brain. *Lab Anim Sci*, 47(1):50–7, 1997.

[52] L. Marzella and A. Yin. Role of Extravascular Gas Bubbles in Spinal Cord Injury Induced by Decompression Sickness in the Rat. *Exp Mol Pathol*, 61(1):16–23, 1994.

[53] Y. Manabe, K. Sakai, K. Kashihara, and T. Shohmori. Presumed venous infarction in spinal decompression sickness. *AJNR Am J Neuroradiol*, 19(8):1578–80, 1998.

[54] T.J.R. Francis, G.H. Pezeshkpour, A.J. Dutka, J.M. Hallenbeck, and E.T. Flynn. Is There a Role for the Autochthonous Bubble in the Pathogenesis of Spinal Cord Decompression Sickness? *J Neuropathol Exp Neurol*, 47(4):475–487, 1988.

[55] L. Marzella and A. Yin. Role of Ischemia in Rats with Spinal Cord Injury Induced by Decompression Sickness. *Exp Mol Pathol*, 62(1):22–27, 1995.

[56] R. Alvarado and C. Hodges and J. Sukovich and J.M. Greve and J.-C. Meiners. Raw data for mechanical damage to spinal cord tissue from decompression bubble expansion. *Univ Michigan – Deep Blue*, 2024.

[57] M. Peksen. *Multiphysics Modelling of Structural Components and Materials*. Academic Press, 2001.

[58] D.E. Yount and R.H. Strauss. Bubble formation in gelatin: A model for decompression sickness. *J Appl Phys*, 47(11):5081–5089, 1976.

[59] C.A. Ward, A. Koheil, D. McCullough, W.R. Johnson, and W.D. Fraser. Activation of complement at plasma-air or serum-air interface of rabbits. *J Appl Physiol*, 60(5):1651–1658, 1986.

[60] F.L. Keays. *Compressed air illness, with a report of 3,692 cases*. Deptment of Medicine Publications of Cornell University Medical College, 1909.

[61] A. Naqvi and D. Clarence. A case of decompression illness not responding to hyperbaric oxygen. *J of Intensive Care*, 6(1):29, 2018.

[62] E. Gempp and J.-E. Blatteau. Risk factors and treatment outcome in scuba divers with spinal cord decompression sickness. *J Crit Care*, 25(2):236–242, 2010.

[63] J.C. Dapena, C.A. Lansdorp, and S.J. Mitchell. Persistent extravascular bubbles on radiologic imaging after recompression treatment for decompression sickness: A case report. *Diving Hyperb Med*, 50(4):424–430, 2020.

[64] T.H. Lam and K.P. Yau. Analysis of some individual risk factors for decompression sickness in Hong Kong. *Undersea Biomed Res*, 16(4):283–92, 1989.

[65] A. Tawar and P. Gokulakrishnan. Decompression illness. *J Mar Med Soc*, 21(2):112, 2019.

[66] Newton H.B. and Padilla W. and Burkart J. and Pearl D.K. Neurological manifestations of decompression illness in recreational divers - the Cozumel experience. *Undersea Hyperb Med*, 34, 2007.

[67] R.D. Workman. Calculation of air saturation decompression tables. Technical Report 11-57, US Naval Experimental Diving Unit, 1957.

[68] R.D. Workman. Calculation of decompression schedulesfor nitrogen-oxygen and helium-oxygen dives. Technical Report 6-65, US Naval Experimental Diving Unit, 1965.

[69] P.K. Weathersby, S.S. Survanshi, L.D. Homer, E. Parker, and E.D. Thalmann. Predicting the time of occurrence of decompression sickness. *J Appl Physiol*, 72(4):1541–1548, 1992.

[70] R. Sander. Compilation of Henry's law constants (version 4.0) for water as solvent. *Atmos Chem Phys*, 15(8):4399–4981, 2015.

[71] COMSOL Multiphysics®. *Solid Mechanics Module User's Guide*. COMSOL.

[72] C.J. Kutz, I.J. Kirby, I.R. Grover, and H.L. Tanaka. Aviation Decompression Sickness in Aerospace and Hyperbaric Medicine. *Aerosp Med Hum Perform*, 94(1):11–17, 2023.

[73] I. Gersh, G.E. Hawkinson, and E.N. Rathbun. Tissue and vascular bubbles after decompression from high pressure atmospheres – correlation of specific gravity with morphological changes. *Journal of Cellular and Comparative Physiology*, 24(1):35–70, 1944.

[74] B.A. Hills and B.D. Butler. Size distribution of intravascular air emboli produced by decompression. *Undersea Biomed Res*, 8(3):163–70, 1981.

[75] T.R. Hennessy and H.V. Hempleman. An examination of the critical released gas volume concept in decompression sickness. *Proceedings of the Royal Society of London. Series B. Biological Sciences*, 197(1128):299–313, 1977.

[76] J. Conkin, R.W. Sanders, M.D. Koslovsky, M.L. Wear, A.G. Kozminski, and A.F.J. Abercromby. A Systematic Review and Meta-Analysis of Decompression Sickness in Altitude Physiological Training. *Aerosp Med Hum Perform*, 89(11):941–951, 2018.

[77] P.M. Muehlberger, A.A. Pilmanis, J.T. Webb, and J.E. Olson. Altitude decompression sickness symptom resolution during descent to ground level. *Aviat Space Environ Med*, 75(6):496–9, 2004.

[78] Neal W.P. and Richard G.D. and Petar J.D. and Joel A.D. and James L.C. Annual Diving Report - 2008 Edition. Technical report, Divers Alert Network, 2008.

[79] W. Xu, W. Liu, G. Huang, Z. Zou, Z. Cai, and W. Xu. Decompression Illness: Clinical Aspects of 5278 Consecutive Cases Treated in a Single Hyperbaric Unit. *PLoS ONE*, 7(11):e50079, 2012.

[80] R. Ball. Effect of severity, time to recompression with oxygen, and re-treatment on outcome in forty-nine. *Undersea Hyperb Med*, 20, 1993.

[81] D.C.C. Lam, F. Yang, A.C.M. Chong, J. Wang, and P. Tong. Experiments and theory in strain gradient elasticity. *J Mech Phys Solids*, 51(8), 2003.

[82] H. Gao, Y. Huang, W.D. Nix, and J.W. Hutchinson. Mechanism-based strain gradient plasticity— I. Theory. *J Mech Phys Solids*, 47(6):1239–1263, 1999.

[83] A. Yadav, K.J.E. Matson, L. Li, I. Hua, J. Petrescu, K. Kang, M.R. Alkaslasi, D.I. Lee, S. Hasan, A. Galuta, A. Dedek, S. Ameri, J. Parnell, M.M. Alshardan, F.A. Qumqumji, S.M. Alhamad, A.P. Wang, G. Poulen, N. Lonjon, F. Vachiery-Lahaye, P. Gaur, M.A. Nalls, Y.A. Qi, D. Maric, M.E. Ward, M.E. Hildebrand, P.-F. Mery, E. Bourinet, L. Bauchet, E.C. Tsai, H. Phatnani, C.E.L. Pichon, V. Menon, and A.J. Levine. A cellular taxonomy of the adult human spinal cord. *Neuron*, 111(3):328–344.e7, 2023.

[84] J. Song and Y. Wei. A Method to Determine Material Length Scale Parameters in Elastic Strain Gradient Theory. *J Appl Mech*, 87, 2020.

[85] s. Sharma and M.F. Hashmi. *Partial Pressure Of Oxygen*. StatPearls Publishing, Treasure Island (FL), 2023.

[86] Gerhard A. Holzapfel and Behrooz Fereidoonnezhad. Chapter 5 - modeling of damage in soft biological tissues. In Y. Payan and J. Ohayon, editors, *Biomechanics of Living Organs*, volume 1 of *Translational Epigenetics*, pages 101–123. Academic Press, Oxford, 2017.

[87] M. Stanners, M. O'Riordan, E. Theodosiou, J.-B.R.G. Souppez, and A. Gardner. The mechanical properties of the spinal cord: a systematic review. *The Spine Journal*, 24(7):1302–1312, 2024.

[88] B. Khuyagbaatar, K. Kim, W.M. Park, and Y.H. Kim. Biomechanical Behaviors in Three Types of Spinal Cord Injury Mechanisms. *J Biomech Eng*, 138(8):081003, 2016.

[89] B. Davies, S. Schaefer, A.R. Fard, V. Newcombe, and M. Sutcliffe. Finite Element Analysis for Degenerative Cervical Myelopathy: Scoping Review of the Current Findings and Design Approaches, Including Recommendations on the Choice of Material Properties. *JMIR Biomedical Engineering*, 9:e48146, 2024.

[90] V. Papadopoulou, R.J. Eckersley, C. Balestra, T.D. Karapantsios, and M.-X.Tang. A critical review of physiological bubble formation in hyperbaric decompression. *Adv Colloid Interface Sci*, 191:22–30, 2013.

[91] A. Møllerløkken and S.L. Blogg and D.J. Doolette and R.Y. Nishi and N.W. Pollock. Consensus guidelines for the use of ultrasound for diving research. *Diving Hyperb Med*, 46(1):26–32, 2016.

[92] D.J. Doolette. Venous gas emboli detected by two-dimensional echocardiography are an imperfect surrogate endpoint for decompression sickness. *Diving Hyperb Med*, 46(1):4—10, March 2016.

[93] R.S. Lillo and M.E. MacCallum. Decompression comparison of N2 and O2 in rats. *Undersea Biomed Res*, 18(4):317–31, 1991.

[94] G. Bradski. The OpenCV Library. *DDJ*, 2000.

[95] C.R. Harris, K.J. Millman, S.J.V.D. Walt, R. Gommers, P. Virtanen, D. Cournapeau, E. Wieser, J. Taylor, S. Berg, N.J. Smith, R. Kern, M. Picus, S. Hoyer, M.H.V. Kerkwijk, M. Brett, A. Haldane, J.F.D. Río, M. Wiebe, P. Peterson, P. Gérard-Marchant, K. Sheppard, T. Reddy, W. Weckesser, H. Abbasi, C. Gohlke, and T.E. Oliphant. Array programming with NumPy. *Nat*, 585(7825):357–362, 2020.

[96] P. Virtanen, R. Gommers, T.E. Oliphant, M. Haberland, T. Reddy, D. Cournapeau, E. Burovski, P. Peterson, W. Weckesser, J. Bright, S.J.V.D. Walt, M. Brett, J. Wilson, K.J. Millman, N. Mayorov, A.R.J. Nelson, E. Jones, R. Kern, E. Larson, C.J. Carey,

İ. Polat, Y. Feng, E.W. Moore, J. VanderPlas, D. Laxalde, J. Perktold, R. Cimrman, I. Henriksen, E.A. Quintero, C.R. Harris, A.M. Archibald, A.H. Ribeiro, F. Pedregosa, P.V. Mulbregt, A. Vijaykumar, A.P. Bardelli, A. Rothberg, A. Hilboll, A. Kloeckner, A. Scopatz, A. Lee, A. Rokem, C.N. Woods, C. Fulton, C. Masson, C. Häggström, C. Fitzgerald, D.A. Nicholson, D.R. Hagen, D.V. Pasechnik, E. Olivetti, E. Martin, E. Wieser, F. Silva, F. Lenders, F. Wilhelm, G. Young, G.A. Price, G.-L. Ingold, G.E. Allen, G.R. Lee, H Audren, I. Probst, J.P. Dietrich, J. Silterra, J.T Webber, J. Slavič, J. Nothman, J. Buchner, J. Kulick, J.L. Schönberger, J.V.D.M. Cardoso, J. Reimer, J. Harrington, J.L.C. Rodríguez, J. Nunez-Iglesias, J. Kuczynski, K. Tritz, M. Thoma, M. Newville, M. Kümmerer, M. Bolingbroke, M. Tartre, M. Pak, N.J. Smith, N. Nowaczyk, N. Shebanov, O. Pavlyk, P.A. Brodtkorb, P. Lee, R.T. McGibbon, R. Feldbauer, S. Lewis, S. Tygier, S. Sievert, S. Vigna, S. Peterson, S. More, T. Pudlik, T. Oshima, T.J. Pingel, T.P. Robitaille, T. Spura, T.R. Jones, T. Cera, T. Leslie, T. Zito, T. Krauss, U. Upadhyay, Y.O. Halchenko, and Y. Vázquez-Baeza. Author Correction: SciPy 1.0: fundamental algorithms for scientific computing in Python. *Nat Methods*, 17(3):352–352, 2020.

[97] A. Buades, B. Coll, and J.-M. Morel. Non-Local Means Denoising. *IPOL*, 9 2011.

[98] R. Alvarado, U.M. Scheven, and Meiners J.-C. Raw data for real-time imaging of decompression gas bubble growth in the spinal cord of live rats. Univ Michigan – Deep Blue, 2024.

[99] J.B. Eisenkraft. *Anesthesia Equipment St*, chapter Anesthesia vaporizers. W.B. Saunders, 2021.